iScience

CellPress
OPEN ACCESS

Article

Multicolor 3D-dSTORM Reveals Native-State Ultrastructure of Polysaccharides' Network during Plant Cell Wall Assembly

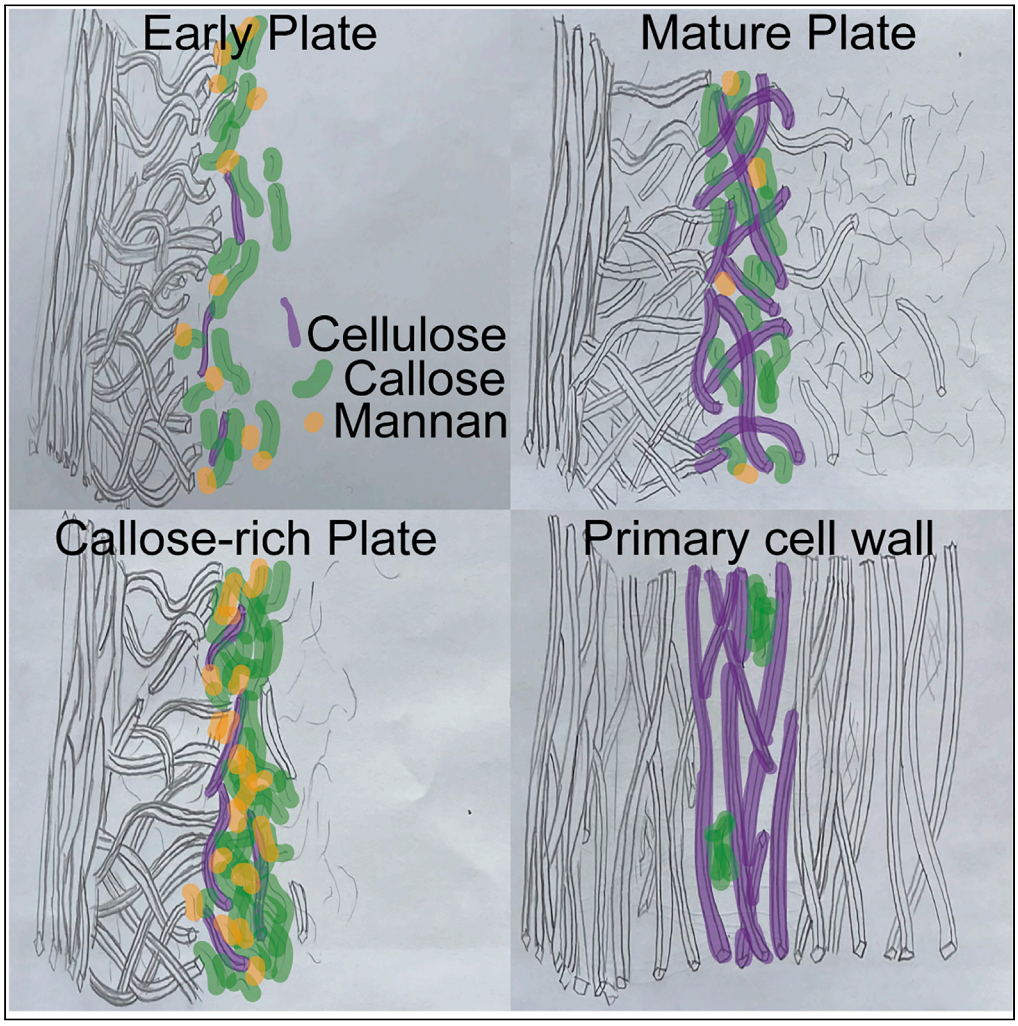

Alexis Peaucelle, Raymond Wightman, Kalina Tamara Haas

kalina.haas@inrae.fr

HIGHLIGHTS

Near-stoichiometric nanoimaging of cell wall polysaccharides

Optimized three-color 3D-dSTORM on sectioned plant tissue

3D Spatial Point Pattern analysis of cell wall probes

Quantitative *in muro* nanoimaging of cellulose, mannan, and callose during cytokinesis

Peaucelle et al., iScience *23*, 101862
December 18, 2020
https://doi.org/10.1016/j.isci.2020.101862

iScience

CellPress
OPEN ACCESS

Article

Multicolor 3D-dSTORM Reveals Native-State Ultrastructure of Polysaccharides' Network during Plant Cell Wall Assembly

Alexis Peaucelle,[1] Raymond Wightman,[2] and Kalina Tamara Haas[1,3,*]

SUMMARY

The plant cell wall, a form of the extracellular matrix, is a complex and dynamic network of polymers mediating a plethora of physiological functions. How polysaccharides assemble into a coherent and heterogeneous matrix remains mostly undefined. Further progress requires improved molecular-level visualization methods that would gain a deeper understanding of the cell wall nanoarchitecture. dSTORM, a type of super-resolution microscopy, permits quantitative nanoimaging of the cell wall. However, due to the lack of single-cell model systems and the requirement of tissue-level imaging, its use in plant science is almost absent. Here we overcome these limitations; we compare two methods to achieve three-dimensional dSTORM and identify optimal photoswitching dyes for tissue-level multicolor nanoscopy. Combining dSTORM with spatial statistics, we reveal and characterize the ultrastructure of three major polysaccharides, callose, mannan, and cellulose, in the plant cell wall precursor and provide evidence for cellulose structural re-organization related to callose content.

INTRODUCTION

The plant cell wall plays key roles in environmental interactions, stress responses, cell-to-cell communication, growth, and morphogenesis. In dividing cells, the completion of mitosis, termed cytokinesis, relies on constructing the cell plate, an intracellular precursor to the cell wall separating the two future daughter cells. The nascent plate assembles as a labile, callose-rich lamella that is subsequently reinforced and replaced with other polymers to form a rigid primary cell wall and so marking the completion of cell division (Drakakaki, 2015). Resolving the native cell plate nanoarchitecture will give insights into the early stages of a 3D polymer network organization that precedes the mature primary cell wall. The composition, architecture, and molecular interaction of hydrogels, such as the cell wall and cell plate, define their biophysical and material properties (Abou-Saleh et al., 2018). The mature primary cell wall has to be strong to sustain a high turgor and allow for remodeling during growth (Chebli et al., 2012). How the cell wall acquires and maintains these sophisticated properties constitutes a fundamental question in plant cell biology. Understanding the *in muro* cell wall assembly will help elucidate this enigma and inspire the next generation of tissue engineering and smart biomimetic materials (Yao et al., 2020). Despite its fundamental importance, the tissue-context native-state three-dimensional organization of the cell wall/cell plate polysaccharides' network remains largely unknown. Established microscopies cannot resolve cell wall polymers in three dimensions without losing molecular specificity or resolution (Chebli et al., 2012). Nowadays, single-molecule localization microscopies (SMLM) permit experimental access in the realm of molecular assemblies in three-dimensions while preserving biochemical specificity. SMLM finally enables observing native-state polymeric and molecular ultrastructure with nanometer precision. Due to technical limitations (tissue-level imaging, strong autofluorescence), its application to plant science is sporadic (Liesche et al., 2013; Eggert et al., 2014; Dong et al., 2015; Haas, et al., 2020b; Haas, et al., 2020a); however, its recent application is already changing the vision of the cell wall structure (Haas, et al., 2020a). Moreover, the biologically relevant three-color 3D nanoscopy implementation, even in simpler isolated cellular systems, is rare.

Here we harness the full potential of SMLM performing three-color 3D dSTORM (direct stochastic optical reconstruction microscopy) on plant tissue. To do so, we identify the optimal combination of photoswitching dyes for triple-color dSTORM in OxEA (Oxyrase-based) (Nahidiazar et al., 2016) buffer compatible with

[1]Institut Jean-Pierre Bourgin, INRAE, AgroParisTech, Université Paris-Saclay, 78000, Versailles, France

[2]Microscopy Core Facility, Sainsbury Laboratory, University of Cambridge, Bateman Street, Cambridge, CB2 1LR, UK

[3]Lead Contact

*Correspondence: kalina.haas@inrae.fr

https://doi.org/10.1016/j.isci.2020.101862

strongly autofluorescent samples. We compare two alternative 3D-dSTORM configurations (1) astigmatic and (2) biplane imaging and evaluate their performance in thin tissue cuts. Using dSTORM nanoscopy we visualize the assembly of three major polysaccharides, cellulose, mannan, and callose, in the nascent cell wall. By employing spatial statistics, we characterize the incorporation, arrangement, proximity, and turnover of these polysaccharides during cell plate development and show their structural transition during plate maturation.

RESULTS

Optimizing the Imaging Conditions for Tissular Multicolor 3D dSTORM

The resolution of the reconstructed SMLM images depends on (1) the labeling density and (2) the localization uncertainties determined by the photon noise, pixel noise, and background noise (Thompson et al., 2002; Mortensen et al., 2010). The dye photoswitching properties, including its brightness, on-off cycle time, and survival time, are critical for gaining high spatial resolution (Dempsey et al., 2011). Therefore, the buffer composition and optimal dye combination for multicolor 3D-dSTORM in biologically relevant applications are essential to maximizing the resolution (Heilemann et al., 2008; Dempsey et al., 2011; Van De Linde et al., 2011; Lehmann et al., 2016; Nahidiazar et al., 2016). Previously we showed a two-color 3D-dSTORM on plant tissue sections using 2F4-GLOX (glucose oxidase-based, 2F4 is a T/Ca/S buffer, see Transparent Methods) buffer (Haas, et al., 2020a, 2020b). Here we tested the OxEA buffer and defined the optimal conditions for three-color 3D-dSTORM observations. We choose Alexa 647 for far-red detection, performing well in both OxEA and GLOX (Lehmann et al., 2016; Nahidiazar et al., 2016; Haas et al., 2018; Haas, et al., 2020a); for red detection, we choose CF568, which displayed superior photoswitching in our modified OxEA buffered with 1 × 2F4 solution. Next, we identified the optimal green dyes, particularly challenging for plant tissue due to strong autofluorescence. Figure 1 presents three-color 3D-dSTORM astigmatic imaging of cell plates from the shoot apical meristem and organ primordia in *Arabidopsis thaliana*. Figure 1A compares a standard 2D pixelated dSTORM image with a coordinate-based scatterplot allowing for three-dimensional "pointillist" data representation and opening a broad avenue for statistical quantifications (Figure S1). To compare photoswitching properties, we imaged four different cell wall epitopes, namely crystalline (CBM3) and amorphous (CBM4) cellulose, hetero-mannans (PDM), and callose after the enzymatic pectin extraction (Haas, et al., 2020b), and tagged them with different fluorescence dyes (Handford et al., 2003; Hernandez-Gomez et al., 2015). Tested dyes, except Alexa 488, displayed very good photoswitching in OxEA at pH 8.5 buffered with a 2F4 solution. This allowed a high-quality super-resolution reconstruction visible in the plots of developing plates characterized by a foam-like structure with voids excluding any of the studied epitope (Figures 1A, 1B, and S2). Green fluorescence dyes such as fluorescein isothiocyanate (FITC), Chromeo 505 (CH505), and CF488 in OxEA, despite the higher autofluorescence in this spectral region (Videos S1–S7), perform as well as either Alexa 647 (A647) or CF568, whereas in the most frequently used GLOX buffer they display no or poor photoswitching (Dempsey et al., 2011). We achieved <10 nm accuracy when determining a fluorophore's position (localization precision) for different dyes and cell wall targets separately, resulting in a resolution of ~40 nm in xy and ~70 nm in z (Figures 1C and S3).

Comparison between Astigmatic and Biplane 3D dSTORM Modalities

Next, we compared the performance of two 3D dSTORM methods, astigmatic and biplane imaging (Huang et al., 2008; Juette et al., 2008). We combined astigmatism with oblique illumination, which confines the imaging section, lowering the out-of-focus signal. In contrast, the biplane imaging uses epifluorescence mode, which can increase the background signal, especially for strongly autofluorescent samples, but allows for deeper observations. Figure 2 shows distinct cell plates for a biplane (A) and astigmatic (B) imaging of callose detected with A647 or CF568 (light-to-dark-blue colormap encodes the z-coordinates), cellulose (CBM3) detected with CH505 or CF488 (orange), or mannan (PDM) detected with CF568. Figure 2C shows the distribution of the axial coordinates of localized fluorophores for both modalities. The z-detection range for astigmatism was <800 nm; in comparison, biplane illumination displayed a ~50% wider z-detection range. The broader and more homogeneous z-detection range is the main advantage of the biplane imaging mode over the astigmatism-based approach. However, astigmatism-based imaging is simpler and more versatile, permitting variable illumination modes: total internal reflection fluorescence microscopy and oblique and epifluorescence illumination. Finally, in our conditions, the biplane approach offered a slight improvement in the axial localization. To achieve a similar axial resolution with astigmatism, we filtered the localization with >2,500 photons (the localization precision scales with the inverse square root of the number of photons) (Figures 2B and S7).

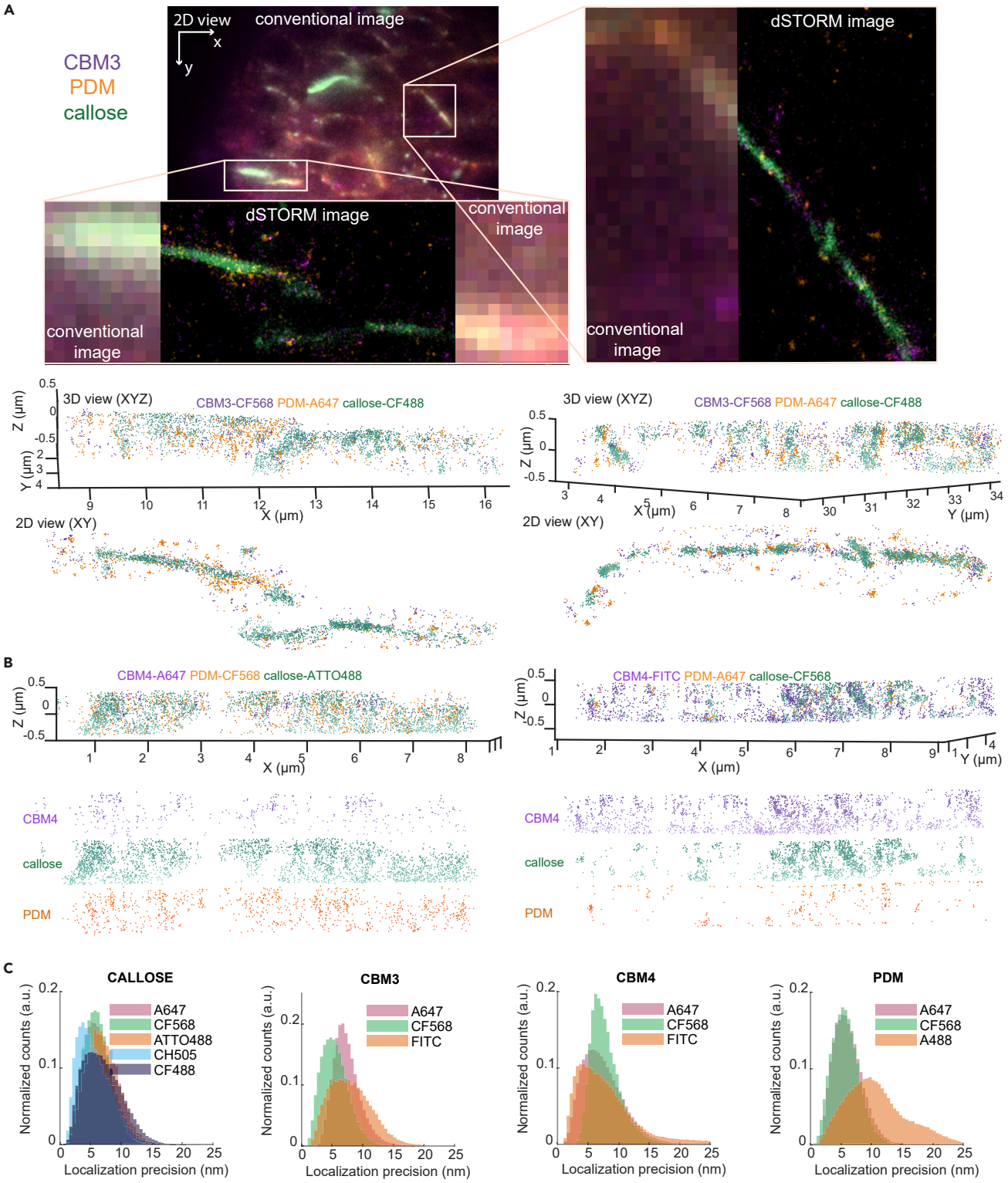

Figure 1. Optimizing Dye Combination for Three-Color 3D-dSTORM

(A) DSTORM data representation as a pixelated 2D image and coordinate-based 3D scatterplots.

(B) Representative cell plates with different epitope-dye combinations showing amorphous cellulose (CBM4, violet), mannan (PDM, orange), and callose (green).

(C) The localization precision distributions for different epitopes and photoswitching dyes. The distributions include localizations with at least 1,500 photons detected.

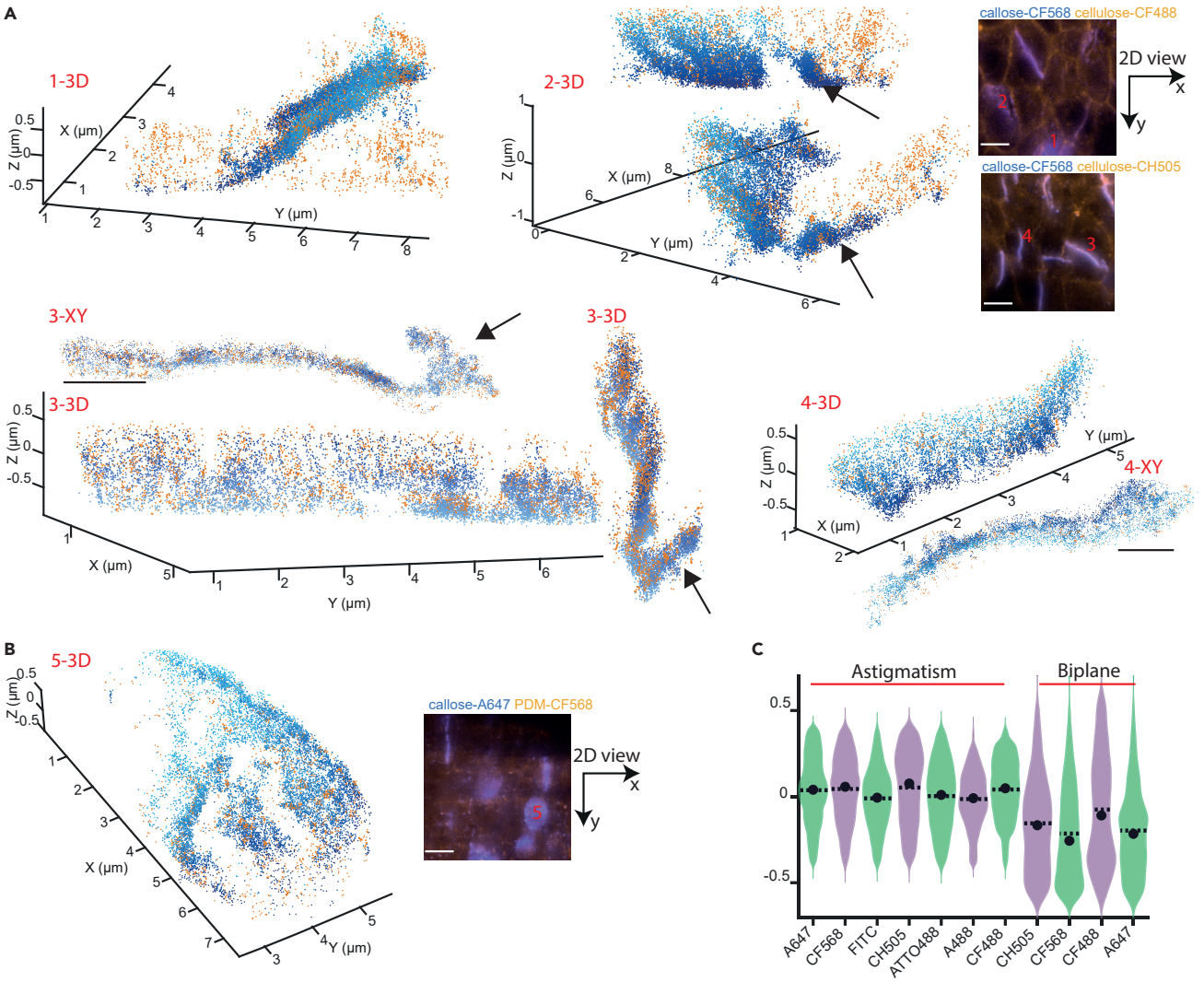

Figure 2. Comparison of Astigmatic and Biplane 3D dSTORM Imaging Modalities

(A–C) Representative cell plates imaged with (A) biplane and (B) astigmatic mode. Orange marks cellulose (CBM3) in (A) and mannan (PDM) in (B). Callose is represented with light-to-dark blue colormap encoding z-position. Data in (A) represent all detected localizations and in (B) localizations with at least 2,500 photons detected. In (A) and (B), the inset images show the conventional oblique illumination pictures of the area imaged with dSTORM. (C) Bean plot of the axial detection range for the astigmatic and the biplane imaging for different photoswitching fluorophores showing all unfiltered localized molecules. The black arrow in (A) indicates a callose-enriched rim protruding from the primary cell wall and directly linked to the developing plate. Scale bars, 1 μm in scatterplot and 5 μm in image.

Visualizing Cell Plate Assembly with Three-Color 3D dSTORM

The different cell plate developmental stages, from the coalescence of the Golgi-derived vesicles and the formation of a membranous tubular network to the maturation stage, have been observed using electron and fluorescence microscopy techniques (Frey-Wyssling et al., 1964; Seguí-Simarro et al., 2004; Baluška et al., 2005; Thiele et al., 2009; Miart et al., 2014; van Oostende-Triplet et al., 2017). However, these techniques lack either molecular specificity or the required resolution to observe the polymers' network in three dimensions. Multicolor 3D-dSTORM allowed us to visualize the polymers' nanoarchitecture and their mutual spatial arrangement in 3D space. Their accumulation level and spatial distribution in dividing cells can serve to discriminate different cell plate developmental stages. First stage is the gradual insertion of polysaccharides, such as callose deposition into small patches (Figure 3, plates 1–4, and Figure S4), that subsequently extend and peak at the fenestrated planar sheet stage (Figure 3, plates 5–6, Figure S5). Accurate determination of the width of this callose-rich sinuous lamella (>∼40 nm, Figure S3D) requires

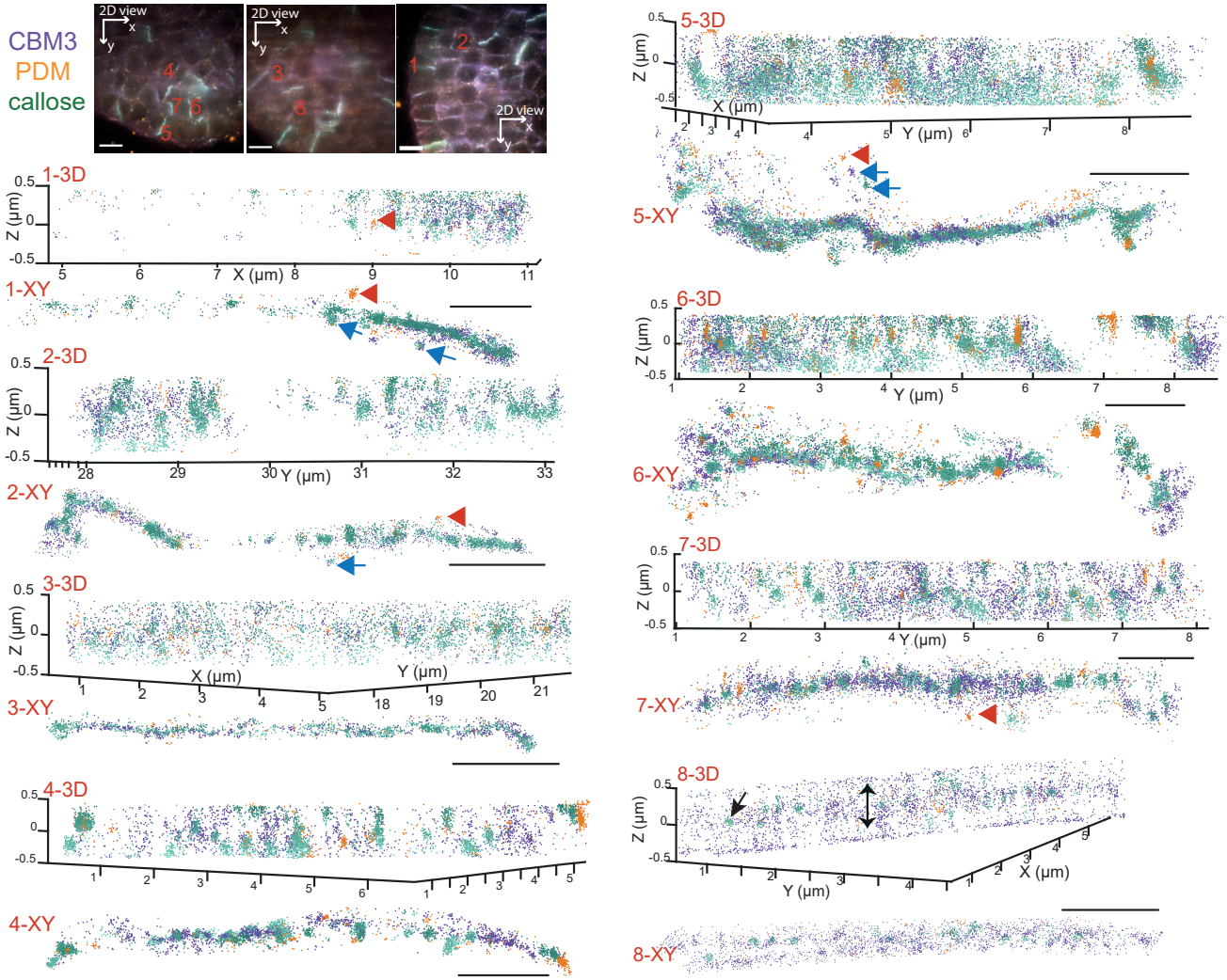

Figure 3. Visualizing Cell Plate Assembly with Three-Color 3D dSTORM

Representative cell plates showing mannan (PDM-CF568, orange), callose-A647 (green), and cellulose (CBM3-FITC, violet). Top row, conventional oblique illumination images with numbers marking cell plates presented below as dSTORM scatterplots shown in two views: top view 2D (xy, the same as low-resolution images above), and side-on 3D view, where the z axis is oriented perpendicular to the conventional image plane. The red arrowheads mark granular structures in close vicinity to the forming plates that may represent mannan-loaded vesicles. The blue arrows show newly synthesized callose and cellulose at the membrane surrounding the forming plate, but could also represent synthesis inside vesicles, as evidenced previously (Chebli et al., 2012). For cell wall #8, double arrow marks vertically aligned aggregates of STORM signal points, corresponding to CBM3 fibers. A black arrow marks callose at a pit. Scale bars, 1 μm for top view plots and 5 μm for low-resolution images.

knowing its orientation in three dimensions; otherwise, the projection errors would lead to >1 μm width measurements (Figure S1B).

In Muro Biochemical Analysis Using the Point Correlation Function

Previous root tip and tobacco cell culture studies showed that the cell plate grows centrifugally, i.e., commencing from the cell center and then outward until meeting with the walls of the parental cell (Samuels et al., 1995; van Oostende-Triplet et al., 2017). Interestingly, we observed that, in the apical meristem and organ primordia, cell plates often protrude from opposite paternal cell walls and accrete at the cell center or grow from just one edge (Figure 3; plates 1, 2, 5, 6, and Figures S4 and S5) (Yang et al., 2016). Next, we estimated statistical dependence between the accumulation of different polymers in the developing plates using pairwise linear regression between the number of detected epitopes. This analysis showed that the accumulation of studied polysaccharides (CBM3/4, PDM, callose) is positively correlated,

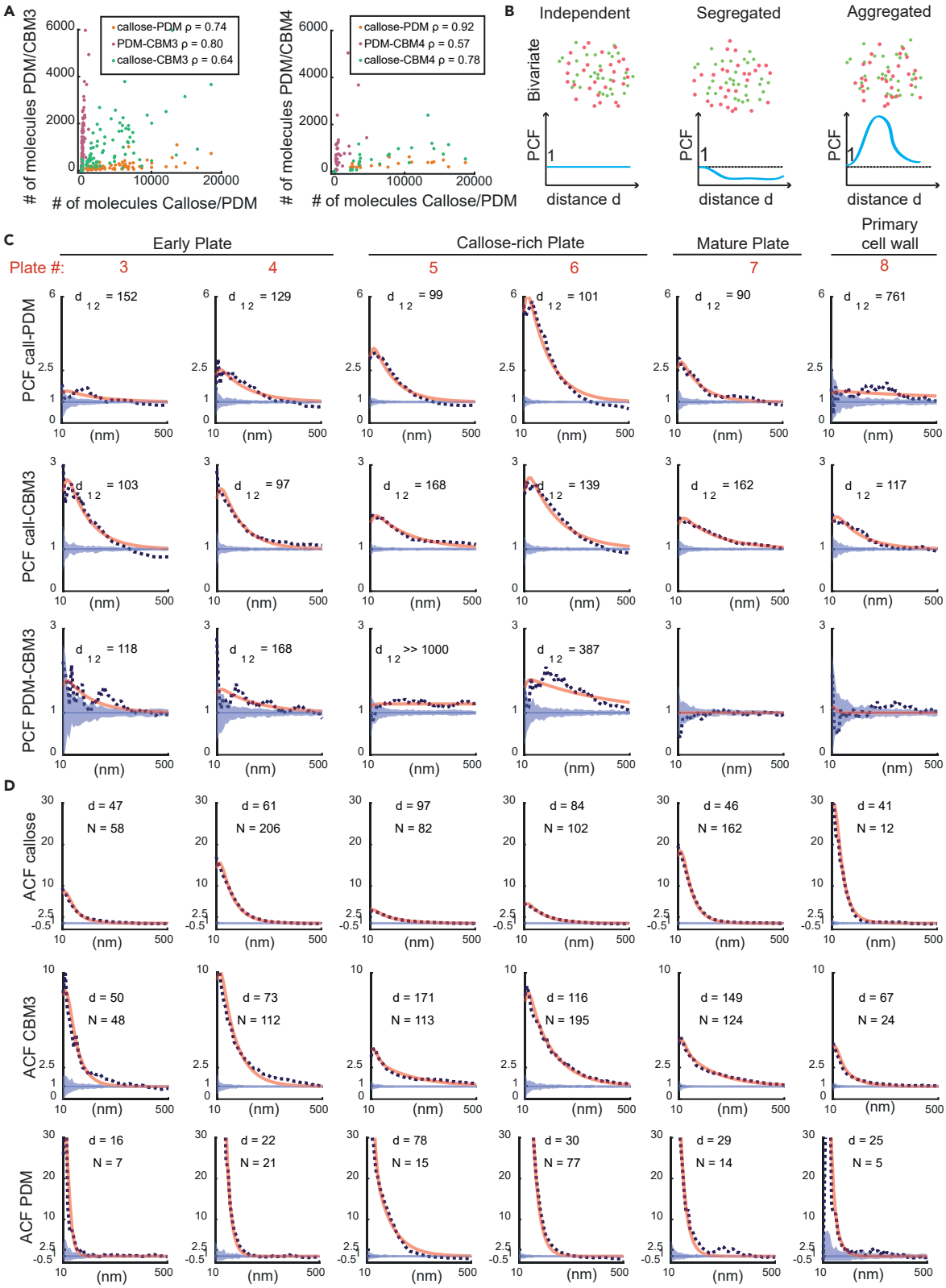
A
callose-PDM ρ = 0.74
PDM-CBM3 ρ = 0.80
callose-CBM3 ρ = 0.64
# of molecules PDM/CBM3
# of molecules Callose/PDM
callose-PDM ρ = 0.92
PDM-CBM4 ρ = 0.57
callose-CBM4 ρ = 0.78
# of molecules PDM/CBM4
# of molecules Callose/PDM
B
Independent
Segregated
Aggregated
Bivariate
PCF
distance d
C
Early Plate
Callose-rich Plate
Mature Plate
Primary cell wall
Plate #: 3 4 5 6 7 8
PCF call-PDM
PCF call-CBM3
PCF PDM-CBM3
d 1 2 = 152
d 1 2 = 129
d 1 2 = 99
d 1 2 = 101
d 1 2 = 90
d 1 2 = 761
d 1 2 = 103
d 1 2 = 97
d 1 2 = 168
d 1 2 = 139
d 1 2 = 162
d 1 2 = 117
d 1 2 = 118
d 1 2 = 168
d 1 2 >> 1000
d 1 2 = 387
(nm)
D
ACF callose
ACF CBM3
ACF PDM
d = 47 N = 58
d = 61 N = 206
d = 97 N = 82
d = 84 N = 102
d = 46 N = 162
d = 41 N = 12
d = 50 N = 48
d = 73 N = 112
d = 171 N = 113
d = 116 N = 195
d = 149 N = 124
d = 67 N = 24
d = 16 N = 7
d = 22 N = 21
d = 78 N = 15
d = 30 N = 77
d = 29 N = 14
d = 25 N = 5

Figure 4. *In Muro* Biochemical Analysis Using the Point Correlation Function

(A) Pairwise linear regression analysis for the relative number of epitopes performed between callose-A647, mannan (PDM-CF568), and crystalline cellulose (CBM3-FITC) for the left panel and the amorphous cellulose (CBM4-FITC) for the right panel; each point represents a cell plate. The legend indicates the Spearman correlation coefficient between pairs of epitopes.

(B) Three different classes of bivariate point patterns and corresponding graphs of PCF. From the left: independent (PCF = 1 at all distances), segregated (PCF <1), and aggregated (PCF >1).

(C) Bivariate pair correlation functions (PCF) for the selected plates shown in Figure 3. The dashed black line marks experimental PCF; the solid blue line and the shaded blue area mark the average PCF and 95% confidence intervals over 25 randomization steps, respectively. The red line marks the fit to exponentially modified Gaussian function; d_{12} is a correlation distance recovered from the fit.

(D) Univariate pair correlation functions (ACF) for the selected plates shown in Figure 3. The dashed black line marks experimental ACF; the solid blue line and the shaded blue area mark the average PCF and 95% confidence intervals over 25 randomization steps, respectively. The red line marks the fit to the sum of Gaussian function and exponentially modified Gaussian function; d is the true domain size and N is the number of molecules per domain recovered from the fit.

concomitant, and not sequential (Figure 4A). Deviation from the linear dependence, especially between callose and cellulose (CBM3 staining), reflects the cell plate maturation stage, going from a "fluid" and wrinkled lamella to a stiff, flat primary cell wall. Callose is digested away during maturation, but cellulose accumulation keeps increasing or levels off (Figure 3; plate, 7).

The "pointillist" dSTORM data permit the quantification using spatial point pattern statistical descriptors to characterize the spatial arrangement of different epitopes (Sengupta et al., 2011; Shivanandan et al., 2016). We developed a boundary-corrected 3D bivariate pair-correlation function (PCF) analysis, commonly used in cosmology. The PCF-based analysis is robust to estimate spatial arrangement and domain size without setting arbitrary thresholds (Sengupta et al., 2011; Veatch et al., 2012; Sengupta et al., 2013). The 3D PCF estimates the number of type 1 molecules within a thin spherical shell centered at the type 2 molecule, normalized to the expected number under the independent distribution. The empirical PCF was compared with the randomized PCF, calculated by the repetitive random reallocation of the experimental points within the 3D boundary enclosing the plate (Figure S8). Randomized distributions have the average PCF = 1, indicating spatial independence between two epitopes (Figure 4B). If the experimental PCF lies above the 95% confidence interval (blue shaded area) at a given distance, it suggests a spatial association. Figure 4C shows that callose with mannan (PDM) and callose with cellulose (CBM3) remain correlated at all developmental stages. At early stages, PDM and CBM3 show nearly independent distribution (Figure 4, plates 3 and 4), which increases during the callose-rich phase, to become again almost independent at the mature plate and primary cell wall stage. Similarly, the correlation between callose and mannan increases from an early stage, peaks at the callose-rich stage, decreases at a mature plate, and becomes nearly independent in the primary cell wall. When applied to the univariate (single molecular species) point patterns, PCF is an autocorrelation function (ACF), which can yield information on the characteristic scales of the molecular assemblies. The effective domain size or the correlation length r_0 can be estimated using a double exponential fit to empirical ACF (Equation 3, Transparent Methods); however, it does not account for single-molecule over-counting, and thus it does not permit stoichiometry evaluation (Figures S8F, S8G, S9, and S10). Due to the natural variability of bound fluorophores, the finite localization precision, and fluorophore blinking, the individual fluorophore appears as a cluster of multiple points (Figures S3E–S3H). Previous reports proposed a model that accounts directly for the fluorophore blinking and the finite localization precision (Sengupta et al., 2011; Veatch et al., 2012; Sengupta et al., 2013), bringing single-molecule imaging to stoichiometric quantification. This model includes the contribution from the multiple detections of a single dye and the target molecule organization, which are convolved with the ACF of the point spread function (see Equation 4, Transparent Methods). This approach estimates the true domain size, *d*, and the average number of molecules, N, present within that domain. This model was developed for PALM, and it does not account for the multiple tagging of the secondary antibodies. When we performed our experiments, the secondary antibodies conjugated to exactly one dye molecule did not exist for all species used in this study. Previous dSTORM applications bypassed this issue by generating control constructs using SNAP and Halo tags that assures precise tag-to-target stoichiometry (Zhao et al., 2014). Unfortunately, polysaccharides cannot be tagged by genetic means. We attempted to estimate the number of conjugated dyes with the spatial clustering using Voronoi diagrams and Delaunay triangulation followed by temporal clustering (Zhao et al., 2014) using kernel density estimates applied to data generated by the isolated secondary antibodies (Figure S3). This analysis shows that the small clusters contain localizations assigned to one temporal cluster (one burst), and the larger clusters contain few temporally separated bursts. The average number of bursts per antibody was 2 for

Alexa 647- and CF568-tagged antibodies and 1 for FITC-tagged antibody, which could serve as a rough estimate of the number of detected dyes.

The effective domain size r_0, the true domain size *d*, and the number of molecules per cluster, N, that we estimated for mannans was r_0 ~28 nm, d ~16 nm, N = 7; r_0 ~30 nm, d ~29 nm, N = 14; and r_0 ~24 nm, d ~25 nm, N = 5 at the early, mature, and primary cell wall stage, respectively; at the callose-rich stage it was r_0 ~70 nm, d ~78 nm, N = 15–77 (Figures 4D and S8; see Transparent Methods for details). This reflects mannans' gradual accumulation and its subsequent removal. However, masking of mannans by other carbohydrates cannot be excluded. Importantly, r_0 ~24 nm corresponds to the value obtained for the single isolated secondary antibody (Figure S8F) and can serve as an estimate for the resolution limited by the localization precision, but not the linkage errors (the size of antibodies' complex). This is supported by the observation that r_0 and *d* are similar for the values >20 nm.

Similar dependencies are observed for callose and cellulose. We observed r_0 ~66 nm/66 nm, d ~47 nm/50 nm; r_0 ~114 nm/187 nm, d ~97 nm/171 nm; r_0 ~64 nm/169 nm, d ~46 nm/149 nm; and r_0 ~48 nm/94 nm, d ~41 nm/67 at the early, callose-rich, mature plate, and primary cell wall stages, respectively, for callose/cellulose. At the primary cell wall stage, the remaining callose patches locate to plasmodesmata that comprise the symplastic connections between the two future daughter cells (Figure 3; cell wall 8, Figure S6). Interestingly, the correlation length of cellulose also decreases between the mature plate and the primary cell wall. This suggests that the cellulose reorganizes from uniform to more fibrous upon callose digestion. These observations agree with *in vitro* studies showing that the addition of callose to cellulose reduces the hydrogel elastic modulus and disrupts the cellulose network (Abou-Saleh et al., 2018). It is further supported by the nanoimaging of callose deposition and its association with cellulose during fungal invasion (Eggert et al., 2014).

Contrary to ACF, PCF is not dependent on the multiple counting of the same dye molecule (Sengupta et al., 2013) and can be modeled by the convolution of exponential decay and the cross-correlation of the point spread functions of each fluorophore (see Equation 6, Transparent Methods). This model permits recovery of the length scale d_{12} at which two molecules are correlated (Figure 4C).

DISCUSSIONS

We demonstrate that multicolor 3D-dSTORM, coupled with statistical quantification, is a powerful bioanalytical tool to study the ultrastructure of cell wall polysaccharides at the tissue level and with molecular specificity. The nanoimaging in three dimensions is indispensable for an accurate reconstruction of the cell wall molecular assemblies and assessing their spatial relationship. 3D-dSTORM permitted cellulose reorganization observations during cell plate maturation, which could explain the mechanical changes between the callose-rich flexible plate and stiff primary cell wall. In the apical meristem, we showed that cell plates often grow out from a "rim" connected to the paternal cell wall, not from the center of the cell as in the root meristem. Moreover, we show that callose, cellulose, and mannan accumulation are concomitant but occur at different rates and results in different final densities. We observed that mannan localizes to small clusters, with the density peaking at the callose-rich stage. The callose accumulation plateaued at the callose-rich stage, whereas the cellulose leveled off at the mature stage. To facilitate the absorption of SMLM into plant science, we optimized buffer/dye combination for three-color imaging and presented two 3D-dSTORM methods, astigmatic and biplane imaging. Due to the distance between epitope and signal (the length of the probe plus antibodies), our resolution (xy~40 nm, z ~70 nm) is not localization precision-limited (~10–20 nm). The development of nanobodies, small tags, and oligosaccharide probes (Mravec et al., 2014) will permit routine dSTORM imaging with single-digit nanometer precision. SMLM technology continuously improves; recently, a new technique, MINFLUX, has demonstrated 1–3 nm localization precision (Gwosch et al., 2020). The combination of dSTORM and expansion microscopy (ex-dSTORM) can further push molecular resolution (Gambarotto et al., 2019). It is reasonable to expect that future experimental advances will bring localization nanoscopy to a genuinely molecular level.

Limitations of the Study

Multicolor 3D dSTORM allows fine mapping of the cell wall polymers' intricate ultrastructure at nanometer-range precision and with biochemical specificity. However, this approach can only map the static, steady-state structure. Moreover, it relies on immunolabeling using full-length primary antibodies conjugated with secondary antibodies that together introduce 15–25 nm linkage errors. The development of smaller

nanoprobes that target cell wall polymers is essential to bring the resolution to a near-molecular level. Furthermore, the application of secondary nanobodies with the precise number of conjugated fluorophores will enable truly stoichiometric imaging. In addition, the 3D Point Pattern Analysis performed in this study did not take into account the anisotropic structure of the studied polysaccharides. Finally, cellulose labeling necessitated enzymatic extraction of pectin that may influence the structure of the studied polysaccharides. In addition, other polysaccharides may still mask some of the target epitopes that were observed in this study.

Resource Availability

Lead Contact

Kalina Tamara Haas kalina.haas@inrae.fr.

Material Availability

This study did not generate any new material.

Data and Code Availability

All software used in this study are available at the GitHub repository https://github.com/inatamara/Grafeo-dSTORM-analysis-. All the dSTORM images will be provided upon request.

METHODS

All methods can be found in the accompanying Transparent Methods supplemental file.

SUPPLEMENTAL INFORMATION

Supplemental Information can be found online at https://doi.org/10.1016/j.isci.2020.101862.

ACKNOWLEDGMENTS

dSTORM experiments were performed at the MRC Laboratory of Molecular Biology, Cambridge, and at the Pasteur Institute Fluorescence Microscopy Workshop III, Paris, and we thank Nick Barry, Jonathan Howe, Michel Biocco, and Marc Koch for their support. We thank Herman Höfte for help with the fundraising and discussion of the results. Funding: A.P. has received the support of the French National Research Agency (ANR) GoodVibration ANR-17-CE13-0007 and of the EU in the framework of the Marie-Curie FP7 COFUND People Program, through the award of an AgreenSkills+ fellowship (under grant agreement no. 201310). The IJPB benefits from the support of Saclay Plant Sciences-SPS (ANR-17-EUR-0007).

AUTHORS CONTRIBUTIONS

K.T.H., A.P., and R.W. designed experiments and wrote the manuscript. A.P. and K.T.H. performed experiments. K.T.H. analyzed the data.

DECLARATION OF INTERESTS

The authors declare no competing interests.

Received: July 29, 2020
Revised: October 7, 2020
Accepted: November 20, 2020
Published: December 18, 2020

REFERENCES

Abou-Saleh, R.H., Hernandez-Gomez, M.C., Amsbury, S., Paniagua, C., Bourdon, M., Miyashima, S., Helariutta, Y., Fuller, M., Budtova, T., Connell, S.D., et al. (2018). Interactions between callose and cellulose revealed through the analysis of biopolymer mixtures. Nat. Commun. *9*, 4538, https://doi.org/10.1038/s41467-018-06820-y.

Baluška, F., Liners, F., Hlavacka, A., Schlit, M., van Cutsem, P., McCurdy, D.W., and Menzel, D. (2005). Cell wall pectins and xyloglucans are internalized into dividing root cells and accumulate within cell plates during cytokinesis. Protoplasma *225*, 141–155.

Chebli, Y., Kaneda, M., Zerzour, R., and Geitman, A. (2012). The cell wall of the Arabidopsis pollen tube-spatial distribution, recycling, and network formation of polysaccharides. Plant Physiol. *160*, 1940–1955.

Van De Linde, S., Löschberger, A., Klein, T., Heidbreder, M., Wolter, S., Heilemann, M., and Sauer, M. (2011). Direct stochastic optical reconstruction microscopy with standard fluorescent probes. Nat. Protoc. *6*, 991–1009.

Dempsey, G.T., Vaughan, J., Chen, K., Bates, M., and Zhuang, X. (2011). Evaluation of fluorophores for optimal performance in localization-based super-resolution imaging. Nat. Methods *8*, 1027–1040.

Dong, B., Yang, X., Zhu, S., Bassham, D.C., and Fang, N. (2015). Stochastic optical reconstruction microscopy imaging of microtubule arrays in intact Arabidopsis thaliana seedling roots. Sci. Rep. *5*, 1–14.

Drakakaki, G. (2015). Polysaccharide deposition during cytokinesis: challenges and future perspectives. Plant Sci. *236*, 177–184.

Eggert, D., Naumann, M., Reimer, R., and Voigt, C.A. (2014). Nanoscale glucan polymer network causes pathogen resistance. Sci. Rep. *4*, 1–6.

Frey-Wyssling, A., López-Sáez, J.F., and Mühlethaler, K. (1964). Formation and development of the cell plate. J. Ultrasruct. Res. *10*, 422–432.

Gambarotto, D., Zwettler, F.U., Le Guennec, M., Schmidt-Cernohorska, M., Fortun, D., Borgers, S., Heine, J., Schloetel J, G., Reuss, M., Unser, M., et al. (2019). Imaging cellular ultrastructures using expansion microscopy (U- ExM). Nat. Methods *16*, 71–74.

Gwosch, K.C., Pape, J.K., Balzarotti, F., Hoess, P., Ellenberg, J., Ries, J., and Hell, S.W. (2020). MINFLUX nanoscopy delivers 3D multicolor nanometer resolution in cells. Nat. Methods *17*, 217–224.

Haas, K.T., Lee, M., Esposito, A., and Venkitaraman, A.R. (2018). Single-molecule localization microscopy reveals molecular transactions during RAD51 filament assembly at cellular DNA damage sites. Nucleic Acids Res. *46*, 2398–2416.

Haas, K.T., Wightman, R., Meyerowitz, E.M., and Peaucelle, A. (2020a). Pectin homogalacturonan nanofilament expansion drives morphogenesis in plant epidermal cells. Science *367*, 1003–1007.

Haas, K.T., Rieviere, M., Wighman, R., and Peaccelle, A. (2020b). Multitarget immunohistochemistry for confocal and super-resolution imaging of plant cell wall polysaccharides. Bio-protocol LLC. *10*, e3783, https://doi.org/10.21769/BioProtoc.3783.

Handford, M.G., Baldwin, T.C., Goubet, F., Prime, T.A., Miles, J., Yu, X., and Dupree, P. (2003). Localisation and characterisation of cell wall mannan polysaccharides in Arabidopsis thaliana. Planta *218*, 27–36.

Heilemann, M., van de Linde, S., Schüttpelz, M., Kasper, R., Seefeldt, B., Mukherjee, A., Tinnefeld, P., and Sauer, M. (2008). Subdiffraction-resolution fluorescence imaging with conventional fluorescent probes. Angew. Chem. Int. Ed. *47*, 6172–6176.

Hernandez-Gomez, M.C., Rydahl, M.G., Rogowski, A., Morland, C., Cartmell, A., Crouch, L., Labourel, A., Fontes, C.M., Willats, W.G., Gilbert, H.J., and Knox, J.P. (2015). Recognition of xyloglucan by the crystalline cellulose-binding site of a family 3a carbohydrate-binding module. FEBS Lett. *589*, 2297–2303.

Huang, B., Wang, W., Bates, M., and Zhuang, X. (2008). Three-dimensional super-resolution imaging by stochastic optical reconstruction microscopy. Science *319*, 810–813.

Juette, M.F., Gould, T.J., Lessard, M.D., Mlodzianoski, M.J., Nagpure, B.S., Bennett, B.T., Hess, S.T., and Bewersdorf, J. (2008). Three-dimensional sub-100 nm resolution fluorescence microscopy of thick samples. Nat. Methods *5*, 527–529.

Lehmann, M., Lichtner, G., Klenz, H., and Schmoranzer, J. (2016). Novel organic dyes for multicolor localization-based super-resolution microscopy. J. Biophotonics *9*, 161–170.

Liesche, J., Ziomkiewicz, I., and Schulz, A. (2013). 'Super-resolution imaging with Pontamine Fast Scarlet 4BS enables direct visualization of cellulose orientation and cell connection architecture in onion epidermis cells', *BMC Plant Biology*. BMC Plant Biol. *13*, 0–8.

Miart, F., Desprez, T., Biot, E., Morin, H., Belcram, K., Höfte, H., Gonneau, M., and Vernhettes, S. (2014). Spatio-temporal analysis of cellulose synthesis during cell plate formation in Arabidopsis. Plant J. *77*, 71–84.

Mortensen, K.I., Churchman, L.S., Spudich, J.A., and Flyvbjerg, H. (2010). Optimized localization analysis for single-molecule tracking and super-resolution microscopy. Nat. Methods *7*, 377–381.

Mravec, J., Kračun, S.K., Rydahl, M.G., Westereng, B., Miart, F., Clausen, M.H., Fangel, J.U., Daugaard, M., Van Cutsem, P., De Fine Licht, H.H., et al. (2014). Tracking developmentally regulated post-synthetic processing of homogalacturonan and chitin using reciprocal oligosaccharide probes. Development *141*, 4841–4850.

Nahidiazar, L., Agronskaia, A.V., Broertjes, J., van den Broek, B., and Jalink, K. (2016). Optimizing imaging conditions for demanding multi-color super resolution localization microscopy. PLoS One *11*, 1–18.

van Oostende-Triplet, C., Guillet, D., Triplet, T., Pandzic, E., Wiseman, P.W., and Geitmann, A. (2017). Vesicle dynamics during plant cell cytokinesis reveals distinct developmental phases. Plant Physiol. *174*, 1544–1558.

Samuels, A.L., Giddings, T.H., and Staehelin, L.A. (1995). Cytokinesis in tobacco BY-2 and root tip cells: a new model of cell plate formation in higher plants. J. Cell Biol. *130*, 1345–1357.

Seguí-Simarro, J.M., Austin, J.R., 2nd, White, E.A., and Staehelin, L.A. (2004). Electron tomographic analysis of somatic cell plate formation in meristematic cells of arabidopsis preserved by high-pressure freezing. Plant Cell *16*, 836–856.

Sengupta, P., Jovanovic-Talisman, T., Skoko, D., Renz, M., Veatch, S.L., and Lippincott-Schwartz, J. (2011). Probing protein heterogeneity in the plasma membrane using PALM and pair correlation analysis. Nat. Methods *8*, 969–975.

Sengupta, P., Jovanovic-Talisman, T., and Lippincott-Schwartz, J. (2013). Quantifying spatial organization in point-localization superresolution images using pair correlation analysis. Nat. Protoc. *8*, 345–354.

Shivanandan, A., Unnikrishnan, J., and Radenovic, A. (2016). On characterizing protein spatial clusters with correlation approaches. Sci. Rep. *6*, 1–12.

Thiele, K., Wanner, G., Kindzierski, V., Jürgens, G., Mayer, U., Pachl, F., and Assaad, F.F. (2009). The timely deposition of callose is essential for cytokinesis in Arabidopsis. Plant J. *58*, 13–26.

Thompson, R.E., Larson, D.R., and Webb, W.W. (2002). Precise nanometer localization analysis for individual fluorescent probes. Biophys. J. *82*, 2775–2783.

Veatch, S.L., Machta, B.B., Shelby, S.A., Chiang, E.N., Holowka, D.A., and Baird, B.A. (2012). Correlation functions quantify super-resolution images and estimate apparent clustering due to over-counting. PLoS One *7*, https://doi.org/10.1371/journal.pone.0031457.

Yang, W., Schuster, C., Beahan, C.T., Charoensawan, V., Peaucelle, A., Bacic, A., Doblin, M.S., Wightman, R., and Meyerowitz, E.M. (2016). Regulation of meristem morphogenesis by cell wall synthases in arabidopsis. Curr. Biol. *26*, 1404–1415.

Yao, J., Fang, W., Guo, J., Jiao, D., Chen, S., Ifuku, S., Wang, H., and Walther, A. (2020). Highly mineralized biomimetic polysaccharide nanofiber materials using enzymatic mineralization. Biomacromolecules *21*, 2176–2186.

Zhao, Z.W., Roy, R., Gebhardt, J.C., Suter, D.M., Chapman, A.R., and Xie, X.S. (2014). Spatial organization of RNA polymerase II insidea mammalian cell nucleus revealed by reflected light-sheet superresolution microscopy. Proc. Natl. Acad. Sci. U S A *111*, 681–686.

iScience, Volume *23*

Supplemental Information

Multicolor 3D-dSTORM Reveals Native-State Ultrastructure of Polysaccharides' Network during Plant Cell Wall Assembly

Alexis Peaucelle, Raymond Wightman, and Kalina Tamara Haas

Supplementary figures and captions

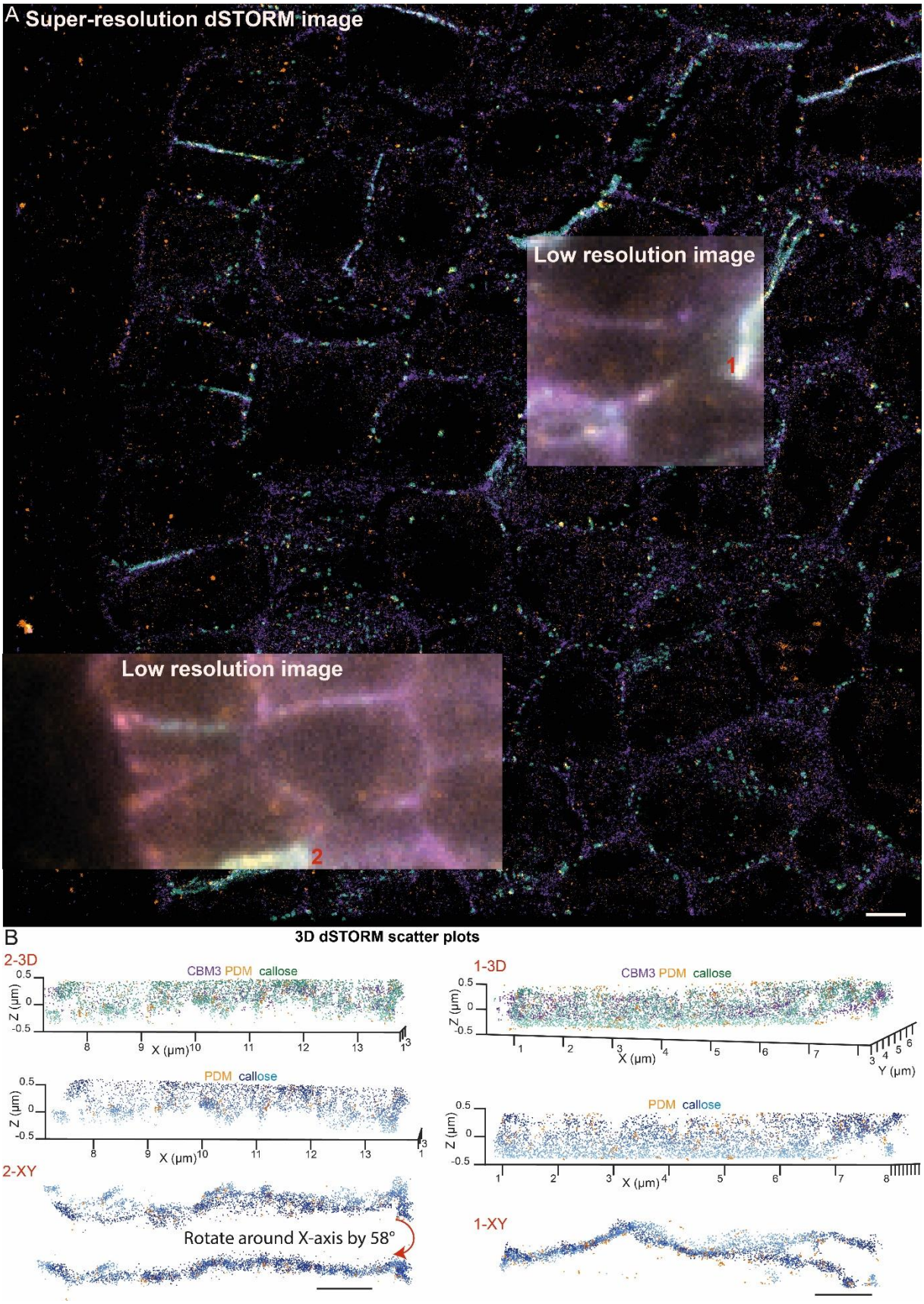

Supplementary fig. 1 Comparison of 3D dSTORM data representation. Related to Figure 1.

The 3D dSTORM data set is comprised of the XYZ coordinates of localized molecules. XY coordinates can be binned to 2D histogram (pixelated image) and represented as (A) super-resolved dSTORM image, here showing Arabidopsis meristem stained against mannan (PDM-CF568, orange), callose-A647 (green), and cellulose (CBM3-FITC, violet). Two superimposed image patches correspond to a low-resolution image. Scale bar, 1 µm. (B) Three-dimensional scatter plot represents two cell plates marked in A) as 1 and 2. Plate #2 is shown in three views: side-on 3D view, top XY view, and top XY view rotated by 58° around X-axis. Z-axis is oriented perpendicular to the image plane shown in A). Two enhance depth perception, the two-color scatter plots show callose in dark-to-light blue colormap and PDM in orange. Scale bar for top view plots and image, 1 µm.

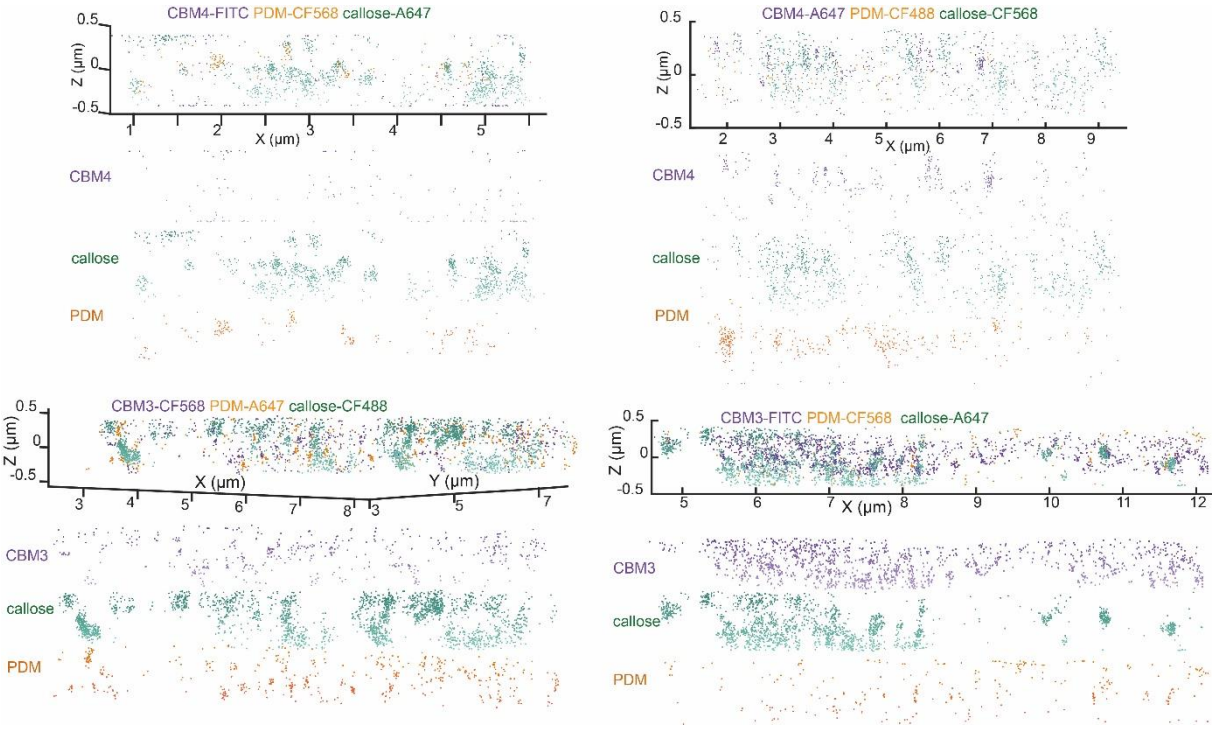

Supplementary fig. 2 Scatter plots of 3D dSTORM coordinates of localized molecules showing representative cell plates with different epitope-dye combinations: CBM4 (violet) PDM (orange), and callose (green). Related to Figure 1.

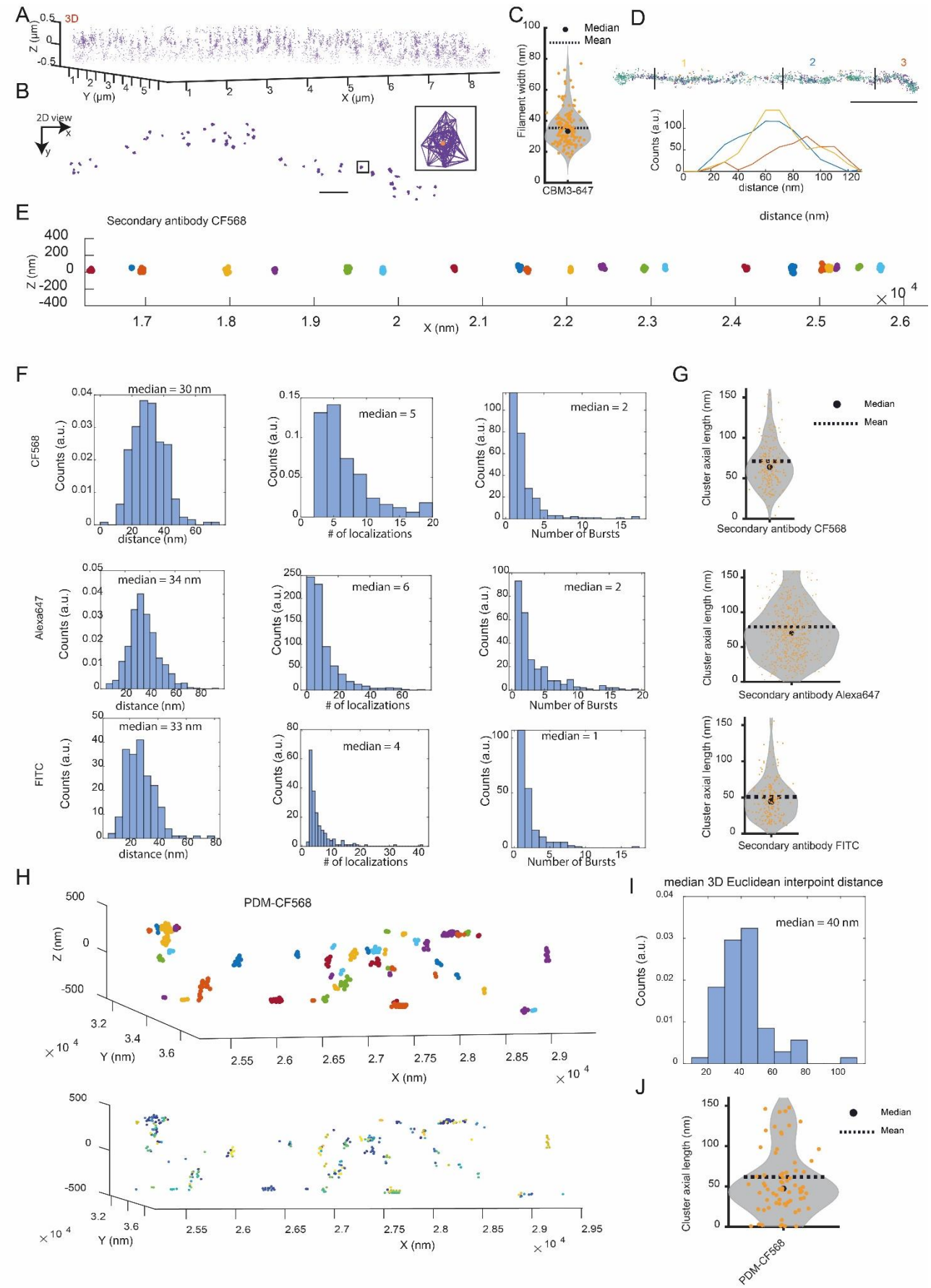

Supplementary fig. 3 Estimating 3D dSTORM resolution and single molecule over-counting. Related to Figures 1-3.

A) Representative primary cell wall region with crystalline cellulose tagged using the CBM3 probe, presenting a fibrous pattern. B) The CBM3 filaments were segmented using 3D Voronoi diagrams and 3D Delaunay triangulation, as described in the Transparent Methods. The lateral resolution was evaluated as a cellulose microfiber's width, estimated as a median radial distance from every point in a connected graph to the graph centroid (orange dot in the bottom zoomed-in graph). C) Bean plot showing the distribution of estimated cellulose microfiber width. D) Cross-sectional analysis of the thin cell plate width. The cross-section was calculated from the Z-projected plots binned to 2D image with a pixel size 10 nm and smooth using ImageJ software. E) The isolated secondary antibodies tagged with CF568 clusters segmented using 3D Voronoi diagrams and 3D Delaunay triangulation as described in the Transparent Methods. Color codes for the different clusters. F) From left to right, histograms showing the average 3D Euclidean point-to-point distance within the cluster, the number of localization within the cluster, and the number of temporal bursts within the cluster for the isolated secondary antibodies tagged with CF568 (top) Alexa647 (middle) or FITC (bottom). G) Bean plots showing the full axial length of isolated antibodies labeled with CF568 (top), Alexa647 (middle), or FITC (bottom). The axial resolution was evaluated as the full axial length of clusters from G) and was around 60-70 nm. H) The PDM-CF568 clusters from cell plate #1 shown in the supplementary fig. 1 segmented using 3D Voronoi diagrams and 3D Delaunay triangulation as described in the Transparent Methods; bottom plot shows the same region color-coded for the frame numbers the molecule was localized. I) Histograms showing the average 3D Euclidean point-to-point distance within the cluster of PDM-CF568. J) Bean plot showing the full axial length of segmented PDM-CF568 clusters

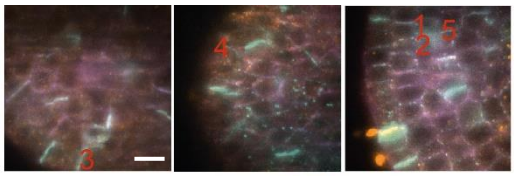

CBM3 PDM callose

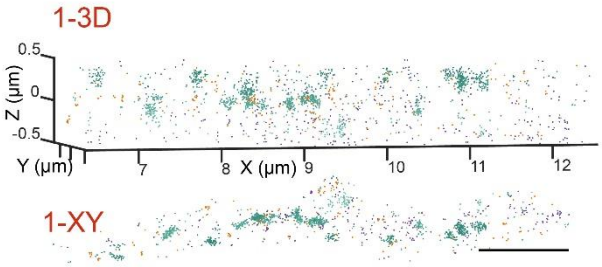

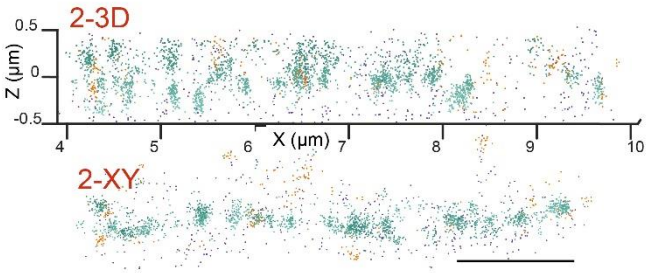

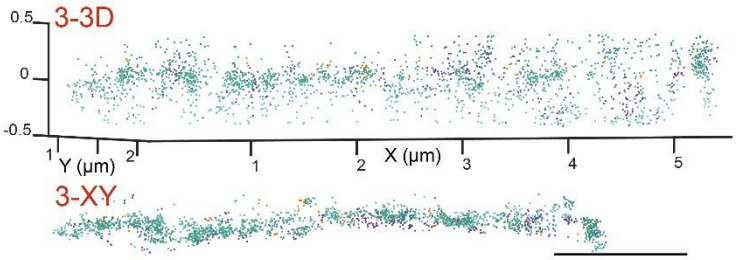

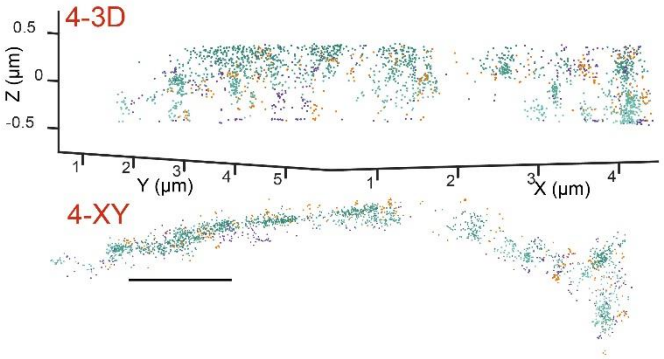

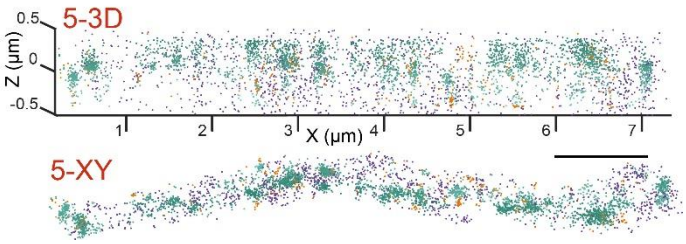

Supplementary fig. 4 Representative cell plates at the early developmental stage showing mannan (PDM-CF568, orange), callose-A647 (green), and cellulose (CBM3-FITC, violet). Related to Figure 3.

The top row shows the conventional oblique illumination image of the area imaged with dSTORM. Each plate is marked by a number on the low-resolution image and shown below as a scattered plot of 3D dSTORM localizations in two views: top view (XY, the same as low-resolution images above), and side-on 3D view, where the z-axis is oriented perpendicular to the conventional image plane. Scale bar for top view plots, 1 µm, and for the image, 5 µm.

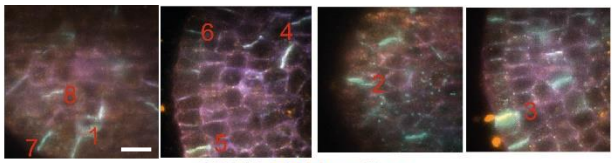
6
4
8
2
7
1
5
3
CBM3 PDM callose

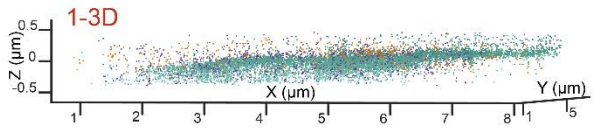
1-3D
Z (µm)
X (µm)
Y (µm)


1-XY

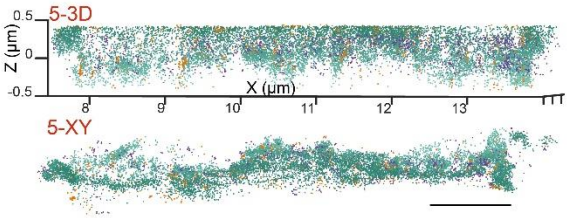
5-3D
Z (µm)
X (µm)
5-XY

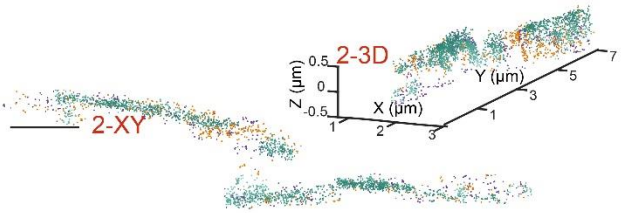
2-3D
Z (µm)
X (µm)
Y (µm)
2-XY

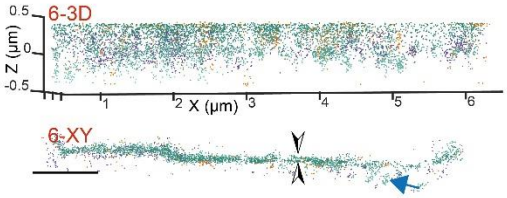
6-3D
Z (µm)
X (µm)
6-XY

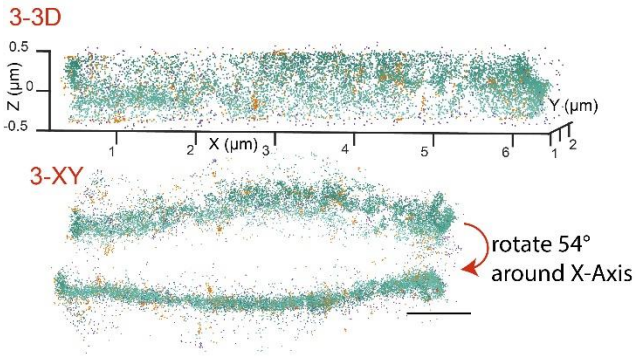
3-3D
Z (µm)
X (µm)
Y (µm)
3-XY
rotate 54°
around X-Axis

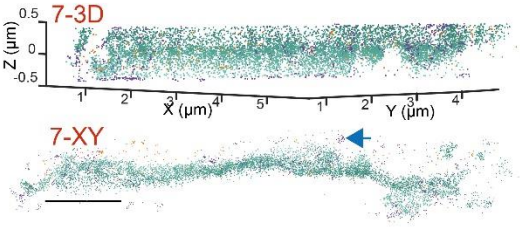
7-3D
Z (µm)
X (µm)
Y (µm)
7-XY

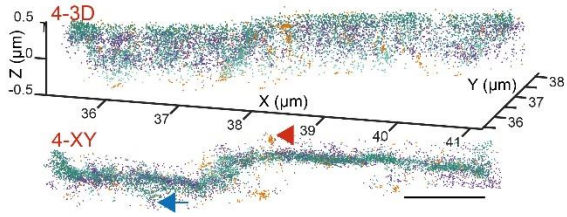
4-3D
Z (µm)
X (µm)
Y (µm)
4-XY

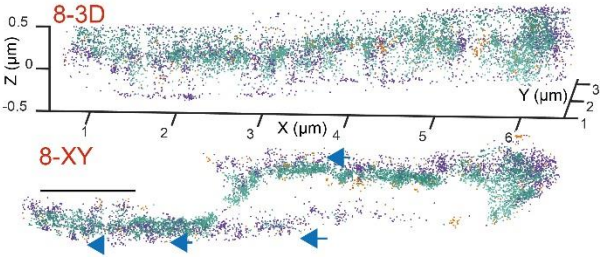
8-3D
Z (µm)
X (µm)
Y (µm)
8-XY

Supplementary fig. 5 Representative cell plates at maturating stage showing mannan (PDM-CF568, orange), callose-A647 (green), and cellulose (CBM3-FITC, violet). Related to Figure 3.

The top row shows the conventional oblique illumination image of the area imaged with dSTORM. Each plate is marked by a number on the low-resolution image and shown below as a scattered plot of 3D dSTORM localizations in two views: top view (XY, the same as low-resolution images above), and side-on 3D view, where the z-axis is oriented perpendicular to the conventional image plane. The red arrowheads mark possible mannan-loaded vesicles; blue arrow - callose and cellulose synthesis sites at the membrane. Plate #3 is shown in three views: side-on 3D view, top XY view, and top XY view rotated by 54° around X-axis. Scale bar for top view plots, 1 µm, and for the image, 5 µm.

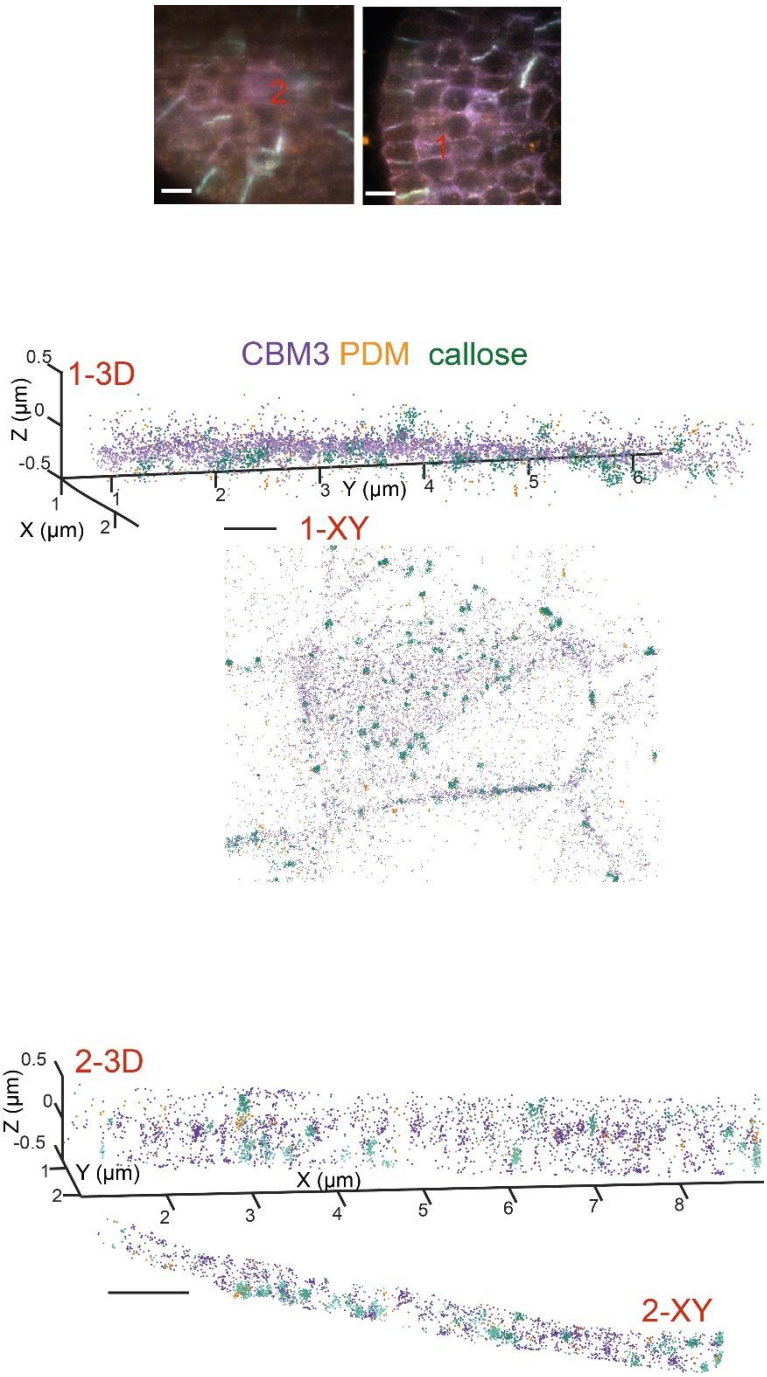

Supplementary fig. 6 Representative mature primary cell wall stage showing mannan (PDM-CF568, orange), callose-A647 (green), and cellulose (CBM3-FITC, violet). Related to Figure 3. Scale bar for scatter plots, 1 µm, and for image, 5 µm.

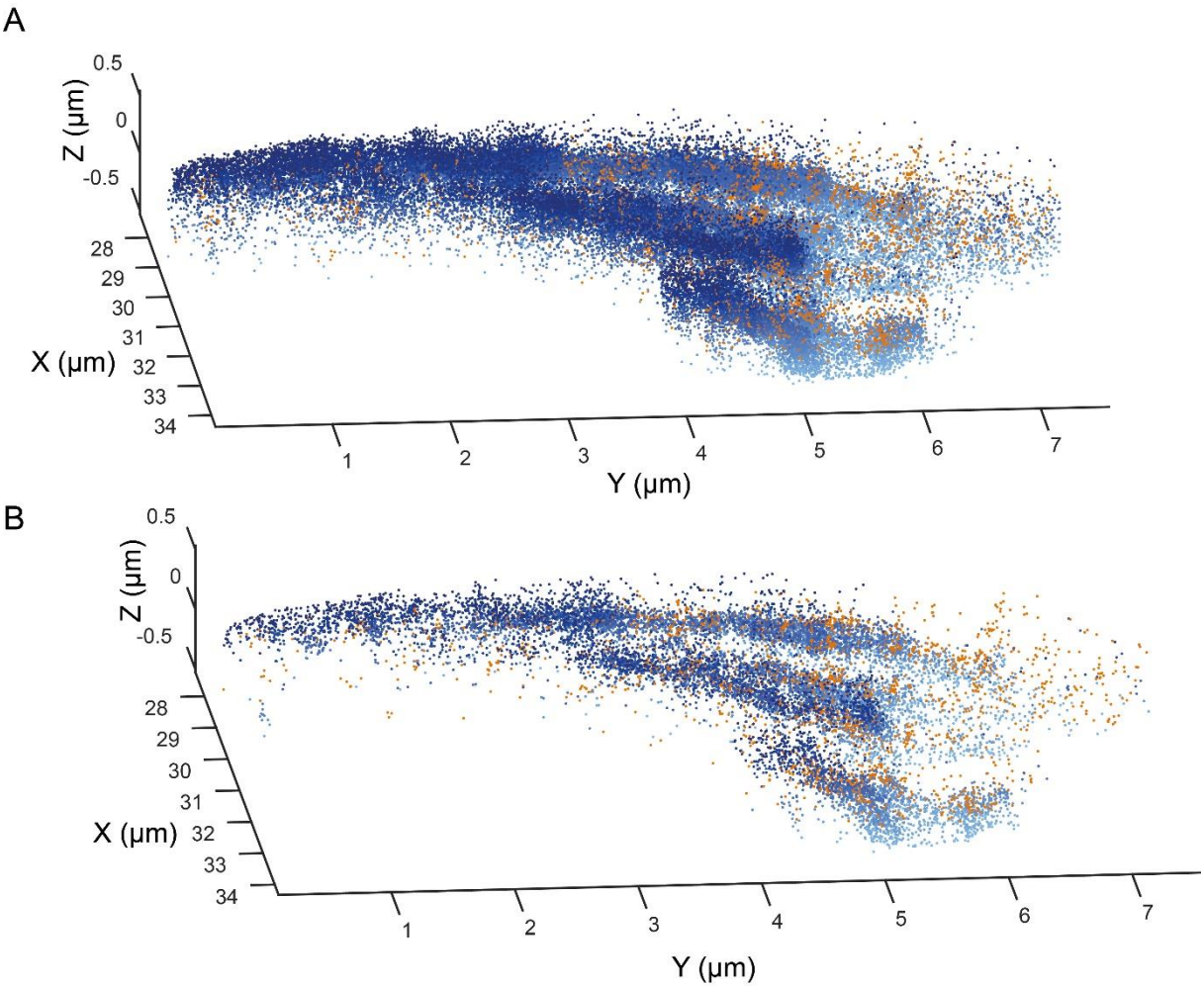

Supplementary fig. 7 Relation between photon counts and effective resolution. Related to Figure 2.

The same plate as shown in fig. 3B before filtering (A) and after filtering out the localized molecules with less than 2500 photons detected. The light-to-dark blue colormap encodes the z-coordinates of callose detected with Alexa647, and orange represents mannan (PDM) detected with CF568. To achieve similar Z-axis resolution and maintain the same detection density, in our condition, astigmatism-based imaging requires the acquisition of more images, as compared to biplane imaging.

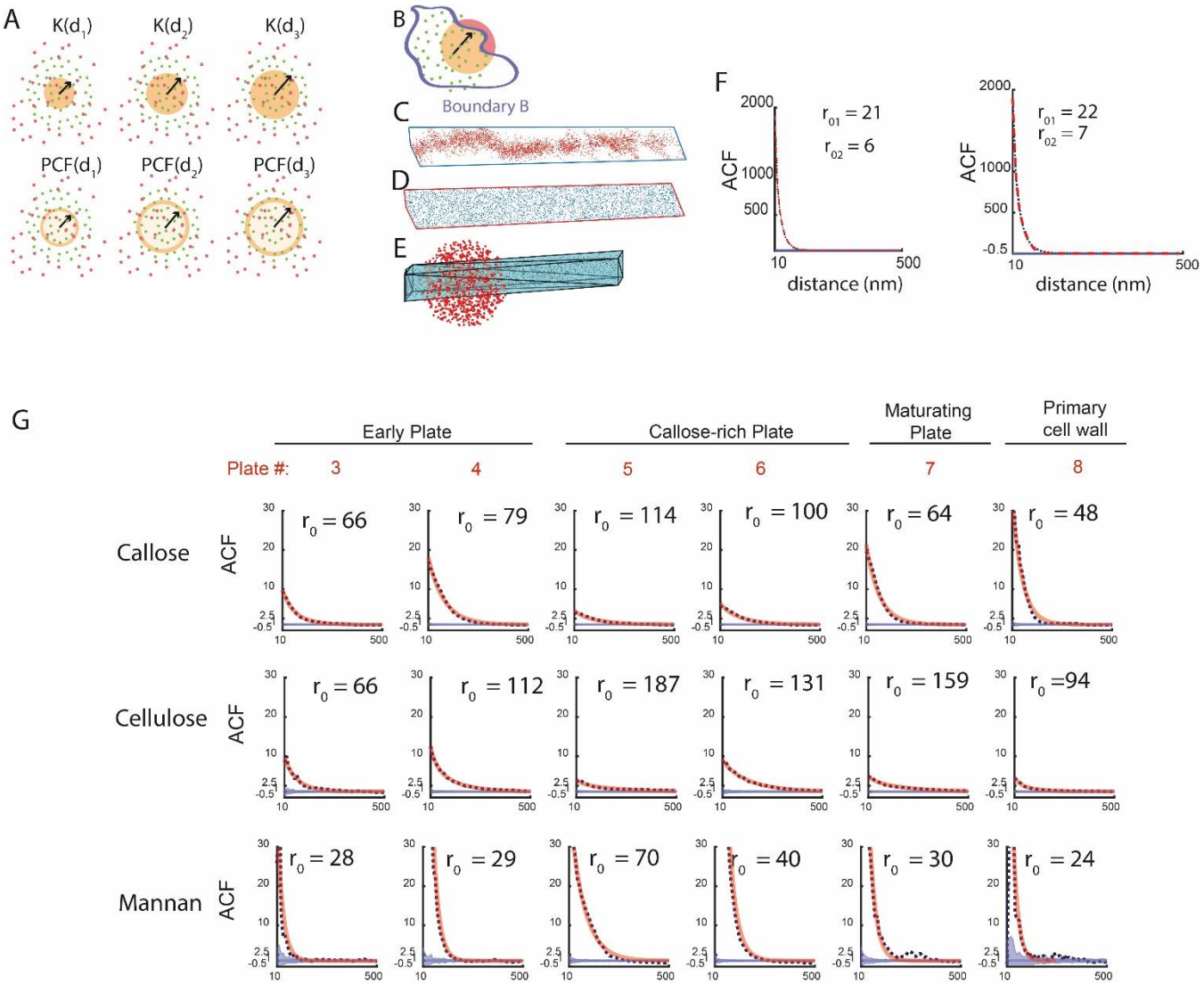

Supplementary fig. 8 The spatial statistics characterization of the cell wall polysaccharides. Related to Figure 4.

A) At a given distance d, a bivariate Ripley's K(d) function is proportional to the expected number of points from pattern 2 contained in a circle (sphere in three dimensions) centered at an arbitrary point from pattern 1 with a radius d. The K(d) is evaluated for a sequence of distances d and usually plotted against d. The point correlation function (PCF) is a derivative of K(d). It can be evaluated as the number of points from pattern 2 in a thin ring (spherical shell in three dimensions) centered at an arbitrary point from pattern 1 with a radius d. B) Cartoon explaining the evaluation of the edge correction factor. Boundary B is an outline of a region within which the pattern is contained. C) 2D view on the experimental data points (red) enclosed by convex 2D polygon B2D. D) Randomization of the experimental points within the boundary B2D. E) Three-dimensional view on the randomized experimental molecular coordinates (black) enclosed by the triangulated boundary B (light blue). The 3D edge correction factor for Ripley's K and PCF functions is the inverse of the fraction of a sphere (circle in 2D) lying inside boundary B. Here it was evaluated as the inverse of the fraction of

randomly generated points bounded by a sphere with a radius d that lies inside the boundary B. (red points), see Transparent Methods.

F) The univariate PCF (the autocorrelation functions, ACF) for the single isolated secondary anybody tagged with CF568; (right) r_{01} and r_{02} is a domain size estimated from the double exponential fit (red line), and (left) r_{01} and r_{02} is a domain size estimated from the double Gaussian fit (red line). G) The ACF for the cell plates evaluated in Fig. 4C. r_0 is a domain size estimated from the double exponential fit (red line); only the longer component is reported.

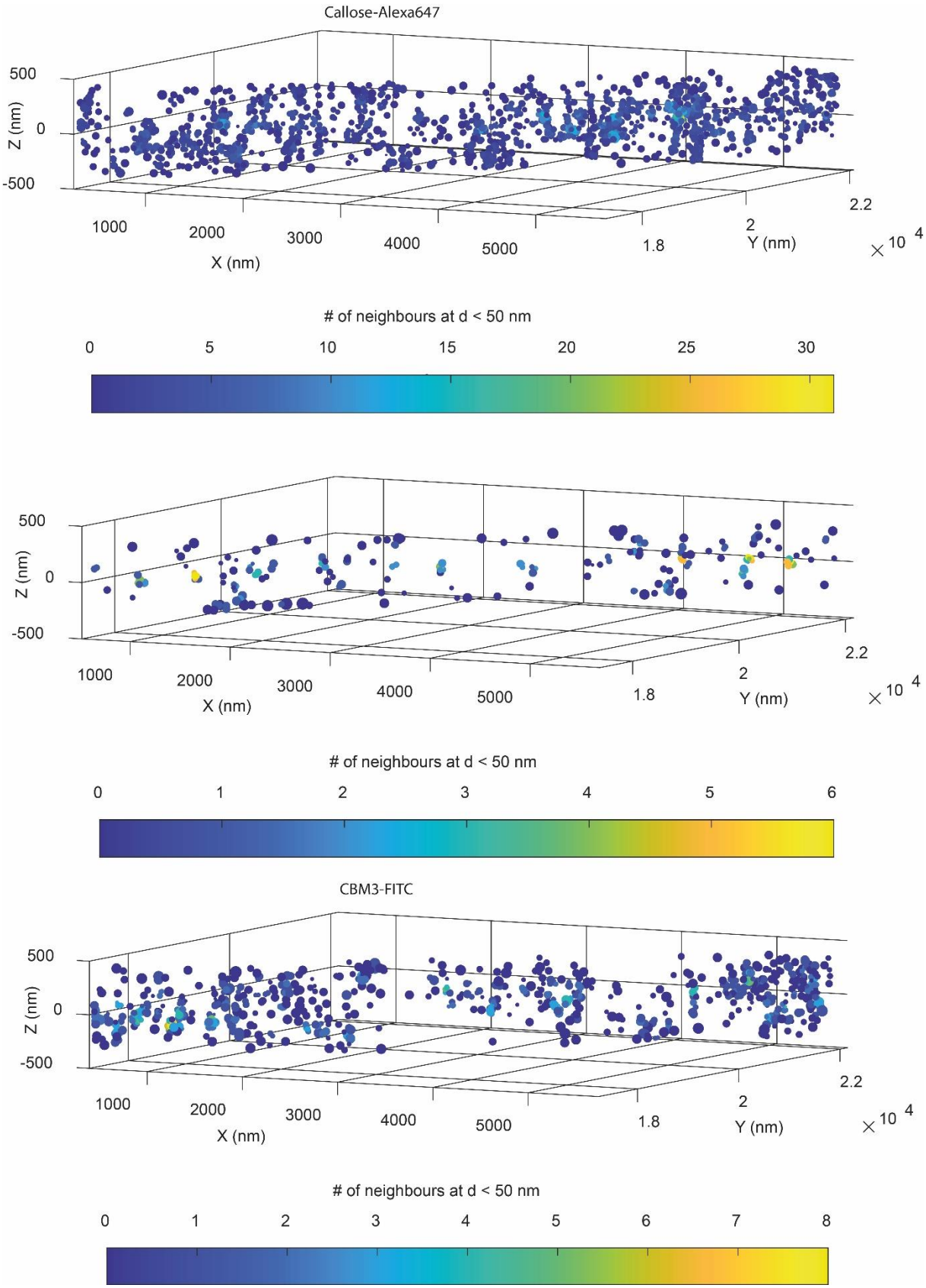

Supplementary fig.9 dSTORM data rendering using localization precision and the number of nearest neighbors. Related to Figure 3.

Scatter plot showing cell plate #3 shown in figure 3. The rendering was generated using the number of nearest neighbors and the localization precision. Colormap marks the number of neighbors at a 3D spherical distance of 50 nm away from a point, and the marker size encodes the localization precision. The distance 50 nm corresponds to the average resolution in 3D and the maximum point-to-point distance set for the Delaunay based cluster segmentation.

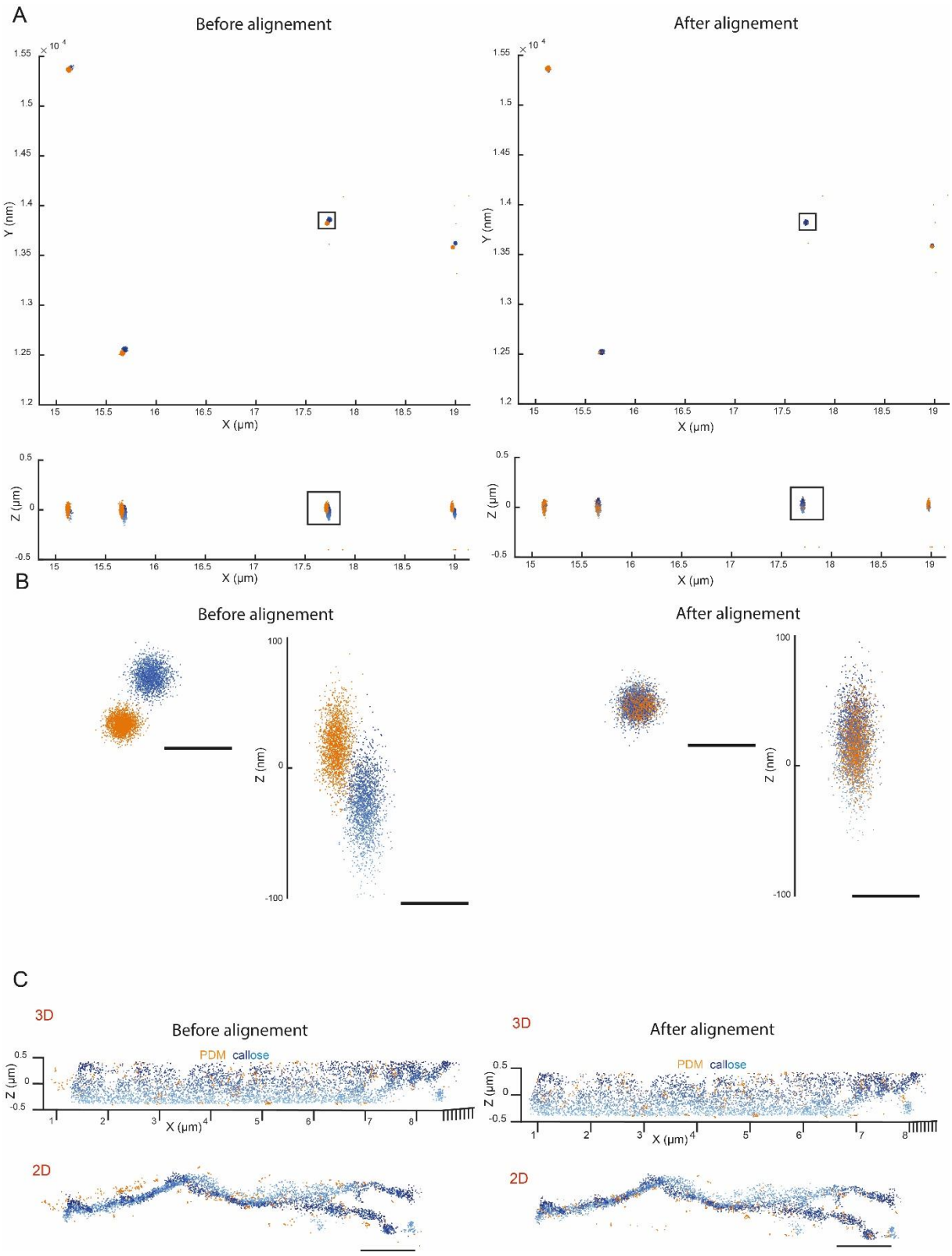

Supplementary fig. 10 Scatter plot color channel registration. Related to Figures 1-3.

Different colors were aligned pairwise (channel 1 with 2, and then channel 1 with 3) by minimizing a 3D Euclidean distance as described in Transparent Methods. A) 3D and 2D scatter plots of multicolor beads before (left) and after (after) alignment B). A selected bead (black rectangle) A) before (left) and after (right) alignment. C) Scatter

plots showing callose (light-to-dark blue colormap encoding z position) and mannan (PDM, orange) before (left) and after (right) alignment.

Transparent Methods

Sample preparation for immunolabelling

Fixation was performed using FAA buffer containing 50% ethanol (CARLO ERBA reagents, catalog number: 4146082), 10 % acetic acid (AnalaR NORMAPUR, catalog number: 20099.324), and 5 % formaldehyde (Sigma-Aldrich catalog number: F1635) for 1 h at room temperature. Samples were dehydrated by incubating in successive ethanol dilutions for at least 30 min each: 70%, 95%, and twice 100%. In the following step, samples were incubated in ethanol diluted with 50% Histo-Clear (Fisher Scientific, HS-200-1GAL, CAS number: 5989-27-5) for 1 h, and then 100% Histo-Clear 1 h. Next, samples were transferred to biopsy cassette (IP-Biopsy-Cassette-III, Leica Biosystems). Histo-Clear was replaced with paraffin (Leica Biosystems, ID: em-400-embedding-medium-paraffin) by incubation in the following paraffin/Histo Clear mixtures: 50% Histo-Clear and 50% paraffin for 3 h, followed by twice 100 % paraffin for 3h, and finally 100% paraffin overnight. Before cutting, samples were stored at 4 °C overnight. Tissue sectioning was performed using a microtome (Biotom Leica Wetzlar, 35578 Germany), after which the tissue cuts were placed in the Ibidi microslide (Ibidi, catalog number: 80827). Next, samples were deparaffined with three successive baths in Histo-Clear, each for 30 min. Then Histo-Clear was removed with a 100% ethanol bath for 20 min. Samples were rehydrated with successive bathing, 15 min each, 100% ethanol, 70% ethanol, 50% ethanol, 25% ethanol, 10% ethanol in 2F4 buffer, and finally 100% 2F4 buffer. A detailed protocol is available at Bio-Protocols (Haas, et al., 2020b).

2F4 (T/Ca/S) specific buffer: 20 mM Tris, 0.5 mM $CaCl_2$, 150 mM NaCl at pH 8.

Immunolabelling

All the immunolabelling steps were performed using a 2F4 buffer. For pectin extraction, before immunostaining, tissue sections were incubated with pectolyase (0.1% w/v, Sigma P3026) in the incubation buffer (0.2M Na_2HPO_4, 0.1M citric acid, pH4.8), as described in (Haas, et al., 2020b) and (Yang *et al.*, 2016). Next, the free aldehyde groups were quenched using 50 mM NH_4Cl (Sigma-Aldrich, catalog number: 254134) in 2F4 buffer for 15 min, and then washed 3 times with 2F4 buffer, each time 3-5 min. The primary antibodies were diluted in the blocking solution containing 1X 2F4 buffer and 5% dried milk (Thermo Fisher Scientific, catalog number: LP0031B). The different primary and secondary antibodies were incubated successively for 2 h at room temperature or overnight at 4 °C. Between each incubation step, samples were washed briefly three times in a blocking solution. For the 8-well Ibidi micro slide, we used 100 µl of antibody solution per well and 500 µl blocking solution for washing steps. After immunolabeling, samples were fixed in 3.7 % formaldehyde in 1X 2F4 buffer for 10 min, washed three times briefly using 1X 2F4 buffer, followed by 15 min incubation using 50 mM NH_4Cl in 2F4 buffer, and then washed briefly three times in 2F4 buffer.

The following primary antibodies were used: CMB3a Crystalline cellulose-binding module, his-tagged, and recombinant CBM protein (Plant Probes, CMB3a) (Blake *et*

al., 2006; Hernandez-Gomez *et al.*, 2015). Anti-His tag polyclonal antibody produced in chicken, Anti-6X-His tag (Abcam, ab9107). Rabbit PDM antibody against mannan was a kind gift by Paul Dupree (Handford *et al.*, 2003; Yang *et al.*, 2016). For availability, please contact raymond.wightman@slcu.cam.ac.uk. Recombinant and His-tagged CBM4 of Cellulomonas fimi (ATCC 484) endoglucanase C ($CBD4_{N1}$) was produced from E. Coli. CBM4 and was a kind gift by Harry Gilbert (Johnson *et al.*, 1996; Blake *et al.*, 2006). For availability, please contact raymond.wightman@slcu.cam.ac.uk. Mouse monoclonal IgG anti- (1→3)-β-Glucan (anti callose) antibody (Biosupplies, 400-2). Antibody dilution: CBM3a/CBM4- 2:100, PDM – 1:100, Callose – 1:100.

The following secondary antibodies were used: Goat anti-mouse F(ab)'2 secondary antibody fragment conjugated to CF568 (Sigma, SAB4600400). Goat anti-mouse F(ab')2 secondary antibody fragment conjugated to Alexa Fluor 647 (Stratech Scientific, 115-607-003-JIR). Donkey anti-mouse F(ab')2 secondary antibody fragment conjugated to Alexa Fluor 647 (Abcam, ab181292). Goat anti-mouse F(ab')2 secondary antibody fragment conjugated to ATTO488 (Hypermole, 2402-0.5MG). Goat anti-mouse IgG conjugated to Chromeo 505 (Activemotif, 15030). Goat anti-mouse F(ab)'2 secondary antibody fragment conjugated to CF488 (Sigma**,** SAB4600388). Goat anti-rabbit F(ab')2 secondary antibody fragment conjugated to Alexa Fluor 647 (Invitrogen, A-21246). Goat anti-rabbit CF568 conjugated F(ab')2 secondary antibody fragment (Sigma, SAB4600310). Goat anti-rabbit Alexa 488 F(ab')2 secondary antibody fragment (Sigma, SAB4600310). Donkey anti-Chicken F(ab')2 secondary antibody fragment conjugated to Alexa Fluor 647 (Jackson immunoresearch, 703-606-155). Donkey anti-Chicken F(ab')2 secondary antibody fragment conjugated to FITC (Jackson immunoresearch, 703-096-155). Goat Anti-Chicken IgY (IgG) (H+L) whole antibody conjugated to CF568 (Biotum, 20104). All the secondary antibodies were used with 1:100 dilution.

Plant growth condition

Arabidopsis meristem was harvested from a plant grown on soil in the long-day condition in the growing chamber and harvested when the inflorescence was 1 cm long; flowers with visible sepals were removed, keeping all the closest flower buds as described in (Haas, et al., 2020b) and (Yang *et al.*, 2016).

Direct Stochastic Optical Reconstruction Microscopy (d-STORM)

Astigmatism-based 3D dSTORM

Samples were imaged at room temperature in an open 8-well ibidi µ-slides by direct STORM on an inverted N-STROM microscope (Nikon Ti, Japan) in highly inclined illumination mode using Apochromat 100x/1.49 NA oil immersion objective. Typically ~20,000 frames were acquired using an EMCCD camera (iXon Ultra DU897, Andor) at ~60 fps. Alexa 647 was imaged with 640 nm, CF568 with 561 nm, and green dyes with a 488 nm excitation laser line. The image was acquired with Quad-Band Set for TIRF applications (Chroma, TRF89901, ET – 405/488/561/640 nm) and the additional

single passband emission filters (Chroma): ET600/50 nm (CF568), ET645/75 nm (Alexa647), and ET525/50 (green dyes) were manually placed under the microscope objective to reduce the cross-talk between the detection of the fluorophores.

Biplane imaging 3D dSTORM

Samples were imaged at room temperature in an open 8-well ibidi µ-slides by direct STORM on the Vutara 350 microscope (Bruker Corp.) in biplane illumination mode using 60x/1.2 NA water immersion objective (Olympus) (Juette *et al.*, 2008). Typically, ~20,000 frames image planes were acquired using a digital CMOS ORCA Flash 4.0 camera (Hamamatsu) at ~60 fps. Alexa 647 was imaged with 640 nm, CF568 with 561 nm, and green dyes with a 488 nm excitation laser line.

OxEA dSTORM imaging buffer

dSTORM imaging was performed in a modified OxEA (Nahidiazar *et al.*, 2016) buffer containing: 100 mM MEA-HCL (Sigma, M6500), 3% (v/v) OxyFlour™ (Oxyrase Inc., Bioquote, OF-0005), 20% (v/v) sodium DL-lactate solution (L1375, Sigma) in 10 X 2F4 buffer diluted with distilled water to obtain the final 1X 2F4 buffer at pH 8.5.

Single-molecule localization data analysis

Single-molecule localization analysis for Biplane 3D dSTORM was performed using Vutara SRX 6.02 software. Single-molecule localization analysis for astigmatic 3D dSTORM was performed with the Nikon NIS elements software setting the maximum possible width of a spot to 700 nm and the maximum axial ratio (ratio of elongation in X- and Y- directions) to 2.5. Multicolour fluorescent microbeads were used as fiducial markers to register the images. Z-position calibration and chromatic aberrations corrections were performed using the fiducial markers. The lateral localization precision was calculated for x, and y dimension, and the combined lateral localization precision was computed as $\sigma = \sqrt{(\sigma_x^2 + \sigma_y^2)}$ as reported previously (Mortensen *et al.*, 2010). The remainder of the data analyses were performed with a custom Matlab-based Grafeo program, as described below.

dSTORM data analysis

The molecular localization lists from Nikon N-STORM and Vutara SRX were imported to custom-written Matlab based single-molecule data analysis software available at https://github.com/inatamara/Grafeo-dSTORM-analysis-. The single-molecule localization data was first filtered based on the number of photons emitted, as described previously (Haas *et al.*, 2018; Haas, et al., 2020a). Typically, the minimum number of photons detected was set to 1000-1500 photons. To minimize the background contribution, we employed a 3D Voronoi diagram-based filtering, as

described previously (Haas *et al.*, 2018). Typically, points forming Voronoi Polygons larger than ~10^{-12}~10^{-16} nm^3 were discarded.

The image registration

Following the drift correction and XY warp transformation as described above, the multicolor scatter plot alignment was performed using Grafeo software.

Prior to alignment, scatter plots were filtered based on the photon counts and Voronoi diagram to ensure the noise's minimal impact. We have employed the algorithm that minimizes the 3D Euclidean distance between two sets of localizations using Matlab's built-in function fminunc. The termination tolerance on the first-order optimality and termination tolerance for the solution was 10^{-8}. This approach works well for the epitopes that localize to the same cellular compartment. Otherwise, it requires several multicolor beads present in the image field of view, on which the algorithm will perform the alignment.

Nanofilament halve-width estimation from 3D-dSTORM data

The coordinates of localized molecules were segmented using 3D Voronoi diagrams (VD) and two-dimensional Delaunay triangulation (DT) thresholding using Grafeo (Haas, et al., 2020a). The segmented DT was then converted to bidirectional graphs, i.e., nodes (points) connected by edges. . DT-based segmentation allows the separation of clusters connected by longer edges than intracluster edges. The discrete clusters (filaments) were segmented by removing the DT edges larger than typically 50 nm and excluding nodes connecting with typically less than 3-5 other points. The threshold values were adjusted depending on the noise level. The halve-width of a filament was estimated as the 2D (X, Y) median pairwise distance between every point in a segmented graph and its centroid. The filament halve-width served as an empirical estimate of a lateral resolution in the coordinates-based approach, akin to the FWHM (Full Width in Halve Maximum) of the filament cross-section, which typically estimates lateral resolution in the image-based approach.

Cluster full axial length estimation from 3D-dSTORM data of PDM-CF568

The coordinates of localized molecules were segmented using 3D Voronoi diagrams (VD) and 3D Delaunay triangulation (DT) thresholding edges larger than 50 nm and excluding nodes connecting with typically less than 3-5 other points. The axial cluster full length was estimated as twice the maximum axial (Z) pairwise distance between every point in a segmented graph and its centroid.

Estimation of single-molecule overcounting using spatiotemporal clustering

Overcounting arises from the conjugation of secondary antibodies to multiple fluorophores or when the fluorophore is counted several times due to blinking. Overcounting leads to self-clustering, which is one molecule's appearance as a small cluster comprised of several localizations and with the spread corresponding to the effective resolution (Zhao *et al.*, 2014).

We imaged single isolated antibodies on the glass coverslip in the same imaging condition as that for cell plates to account for the overcounting. The coordinates of localized molecules were segmented using 3D Voronoi diagrams (VD) and 3D

Delaunay triangulation (DT), removing edges larger than 50 nm. Clusters with less than two points were excluded from the analysis. The median number of molecules in such a cluster estimates the median number of localizations generated by the single antibody. It should be noted that a single antibody can be detected only once, but such events were discarded from the cluster analysis. Next, each cluster was subjected to temporal clustering (Zhao *et al.*, 2014), which estimates the number of fluorescence bursts, followed by long dark periods or photobleaching. The temporal proximity of localized molecules within the same cluster was evaluated by fitting probability distribution (PD) to data using nonparametric kernel smoothing with the bandwidth 10 (Matlab function fitdist). The resulting PD was used to calculate the probability density function (PDF) (Matlab function pdf). The number of bursts was estimated as the number of peaks in the PDF detected using Matlab function findpeaks.

Spatial point pattern analysis

Set of points D distributed inside closed and bounded region B is called a spatial point pattern. Here B outlines the cell plate, and D contains events, coordinates of the localized molecules. Bivariate, edge-corrected 3D Pair-Correlation function was implemented in Grafeo software. First, we calculated 3D edge-corrected bivariate Ripley's K function, which at the distance d can be estimated as the number of type l points at a distance not greater than d from randomly chosen type k point. We have used the following estimator for bivariate Ripley's K function (Dixon, 2006):

$$K_{kl}(\mathrm{d}) = (\lambda_k \lambda_l \mathrm{V})^{-1} \sum_k^m \sum_l^n \mathrm{w}(\mathrm{k_i}, \mathrm{l_j}) \mathrm{I}(\mathrm{dij} < \mathrm{d}) \quad (1)$$

Where V is a volume of studied region *B*, l and k denote different event sets (different localized epitopes, e.g., CBM3 and PDM), λ_k and, λ_l is the number of points per unit volume for each event set, *m* and *n* is a number of events in a set l and k respectively, w_{ij} is an edge correction factor. In the three dimensions, w_{ij} can be calculated as a fraction of a ball with a radius d_{ij}, centered at a point i, which lies inside region *B*. Edge correction is the most important for the large distances since large balls are more likely to overhang from the boundary *B*. The bivariate PCF is a derivative of Ripley's K function and here was estimated as the difference between Ripleys' K function at distances d and d + dr, normalized by the difference in a volume of a spherical shell with radius d and the thickness dr:

$$PCF_{kl}(d) = \frac{K(d+dr) - K(d)}{4/3\pi((d+dr)^3 - d^3)} \quad (2)$$

The edge correction in three-dimensions can be very time-consuming, even for a moderate number of points. To optimize the calculation speed, the edge correction factor was implemented as follows: For each point i, we generated 1000 random points bounded by a sphere with coordinates x_i, y_i, z_i, and radius d_{ij}. The edge correction

function was then calculated as an inverse of a fraction of points inside a sphere lying inside the 3D boundary *B*. See also Supplementary fig. 8

If the point patterns k and l are independent, Ripley's function at the distance d equals $4/3\pi d^3$, and the PCF(d) = 1. This simple relation enables to test whether two point patterns are independent (PCF(d) = 1), exhibit aggregation or attraction (PCF(d) > 1), and finally (PCF(d) < 1) suggests repulsion or segregation between members of different event sets. The empirical PCF was compared to the randomized PCF, obtained by repetitive random reallocation of the points inside the boundary B, and calculation of PCF at each step. The 2D outline B_{2D} of a cell plate was drawn by hand as an approximately convex polygon, and the Z-axis lower and upper bounds were set typically at -400 nm to 400 nm to form a 3D convex polyhedron.

Random points generation in a 3D convex polyhedron.

First, the 2D coordinates of random points are generated. For the convex B_{2D}, a Delaunay triangulation is calculated. Next, each triangle area is calculated using a 2x2 determinant method, and the areas are normalized by the area of a 2D polygon B_{2D}. Then, for each randomly picked triangle, one point lying inside this triangle is found. Bigger triangle will have proportionally more points to fall in them. Finally, the Z-coordinate was generated using the Matlab ‘rand’ function. See also Supplementary fig. 8.

Randomization test

We employed the randomization method to assess the significance of the empirical PCF functions' departure from the null hypothesis (the independent distribution for bivariate patterns and the random distribution for univariate patterns). For every randomization step, Ripley's K and then PCF functions are computed. Confidence envelopes are constructed at each step by taking 5% and 95% percentiles from all randomization trials. Significance of the departure from the null hypothesis can be visualized by comparing the plot of empirical functions with upper U(d) (95%) and lower L(d) (5%) simulation envelopes. The Confidence interval is a region between L(d) and U(d) and is represented as a shaded blue area. If an empirical PCF (ACF) is larger than the confidence interval at a given scale, it implies a tendency to aggregate; when the empirical PCF lies below the confidence interval, two sets of points tend to segregate or disperse. Finally, if the empirical PCF overlaps with the confidence intervals, the null hypothesis cannot be rejected, and the two sets of points are spatially independent (random for univariate pattern). The polynomial trend was removed from the empirical and randomized PCF by fitting the polynomial with the degree typically 2

or 3 to the average randomized curve. This resulted in the average randomized PCF centered at y = 1.

Model fitting to ACF and PCF

To recover an effective domain size r_0, a double exponential function was fit to the autocorrelation function (ACF) using Matlab lsqcurvefit function:

$$f = 1 + Aexp^{-r/r_0} + Bexp^{-r/\sigma} \quad (3)$$

Where σ estimates the size of a cluster generated by isolated antibody and was constrained to be below 30 nm. The fit was performed for r =10 nm, to r = 500 nm.

The effect of self-clusterization due to the over-counting of the same molecule and the final localization precision on ACF can be accounted for through fitting the model as described previously (Veatch *et al.*, 2012, Sengupta *et al.*, 2011, Sengupta, Jovanovic-Talisman and Lippincott-Schwartz, 2013):

$$ACF(r)_{tot} = (\frac{\delta(r)}{\rho} + \left(1 + Ae^{-\frac{r}{d}}\right)) \otimes ACF(r)_{PSF} \quad (4)$$

The first term corresponds to the molecule appearance at r = 0 due to the multiple detections of the same fluorescent molecule and described by Dirac delta $\delta(r)$, divided by the average density of molecules ρ. The second term models the molecule organization using the exponential decay, where *d* corresponds to the true domain size. Due to the finite localization precision, both terms are convolved with the autocorrelation function ($ACF(r)_{PSF}$) of the effective point spread function (PSF), where ⊗ denotes convolution operations. The convolution of Dirac delta with PSF mathematically expresses the spread of a single molecule from a single point to an area defined by the localization precision. The PSF can be modeled as a Gaussian function $PSF(r) = \left(\sigma\sqrt{2\pi}\right)^{-1} e^{-\frac{r^2}{2\sigma^2}}$, and its autocorrelation is also a Gaussian function $ACF(r)_{PSF} = \frac{1}{4\pi\rho\sigma^2} e^{-r^2/(4\sigma^2)}$. The convolution of exponentially decaying function ($\frac{1}{d} e^{-\frac{r}{d}}$) with a Gaussian function ($\left(\sigma\sqrt{2\pi}\right)^{-1} e^{-\frac{r^2}{2\sigma^2}}$) is given by the exponentially modified Gaussian function or exGaussian:

$$exG(r) = \frac{1}{d} \exp\left(\frac{\sigma^2}{(2d^2)} - \frac{r}{d}\right)\left(1 + \operatorname{erf}\left(\frac{r - \frac{\sigma^2}{d}}{\sqrt{2}\sigma}\right)\right) \quad (5)$$

Where $\operatorname{erf}(r) = 2/\sqrt{\pi} \int_0^x e^{-z^2} dz$ is an error function corresponding to the area under the Gaussian curve between –x and x.

The model expressed by the eq. 4 accounts for the multiple detections of the same fluorescence dye. dSTORM involves antibody labeling, where secondary antibodies have a variable number of the conjugated fluorophores, which is not accounted for in the first term of Eqn. 4. The equation 4 was fit using Matlab lsqcurvefit function to recover d, and A. Average density ρ was estimated from the dataset using Voronoi diagrams, and σ using localization precision distributions, and σ was typically ~10 nm.

The fit was typically performed for the distances from r =10 nm, to r = 500 nm, but was adjusted for noisy ACF at short distances if necessary. The number of molecules in the domain d can be calculated as follows: $N = 2\pi A d^2 \rho$.

The pair correlation function PCF is not influenced by the over-counting, and it can be fitted with the following model as shown before (Sengupta, Jovanovic-Talisman and Lippincott-Schwartz, 2013):

$$PCF(r) = \left(1 + Ae^{-\frac{r}{d}}\right) \otimes C(r) \quad (6)$$

Where C(r) is a cross-correlation of the two point spread functions corresponding to two imaging channels and is also given by the Gaussian function with the sigma $\sigma_c = \sqrt{\sigma_1^2 + \sigma_2^2}$. The fit was typically performed for r =10 nm, to r = 500 nm. Equation 6 was fit using Matlab lsqcurvefit function to recover d and A.

References

Blake, A. W. *et al.* (2006) 'Understanding the biological rationale for the diversity of cellulose-directed carbohydrate-binding modules in prokaryotic enzymes', *Journal of Biological Chemistry*, 281(39), pp. 29321–29329.

Dixon, P. M. (2006) ' Ripley's K Function ', *Encyclopedia of Environmetrics*, 3(December), pp. 1796–1803.

Haas, K. T. *et al.* (2018) 'Single-molecule localization microscopy reveals molecular transactions during RAD51 filament assembly at cellular DNA damage sites', *Nucleic Acids Research*, 46(5), pp. 2398–2416.

Haas, K. T., *et al.* (2020b) 'Multitarget Immunohistochemistry for Confocal and Super-resolution Imaging of Plant Cell Wall Polysaccharides', *Bio-protocol*, 10(19), p. e3783. doi: 10.21769/BioProtoc.3783.

Haas, K. T., *et al.* (2020a) 'Pectin homogalacturonan nanofilament expansion drives morphogenesis in plant epidermal cells', *Science*, 367(6481), pp. 1003–1007.

Handford, M. G. *et al.* (2003) 'Localisation and characterisation of cell wall mannan polysaccharides in Arabidopsis thaliana', *Planta*, 218(1), pp. 27–36.

Hernandez-Gomez, M. C. *et al.* (2015) 'Recognition of xyloglucan by the crystalline cellulose-binding site of a family 3a carbohydrate-binding module', *FEBS Letters*, 589(18), pp. 2297–2303.

Johnson, P. E. *et al.* (1996) 'Interaction of soluble cellooligosaccharides with the N-terminal cellulose-binding domain of Cellulomonas fimi cenc. 2. NMR and ultraviolet absorption spectroscopy', *Biochemistry*, 35(44), pp. 13895–13906.

Juette, M. F. *et al.* (2008) 'Three-dimensional sub-100 nm resolution fluorescence microscopy of thick samples', *Nature Methods*, 5(6), pp. 527–529.

Mortensen, K. I. *et al.* (2010) ‘Optimized localization analysis for single-molecule tracking and super-resolution microscopy’, *Nature Methods*, 7(5), pp. 377–381.

Nahidiazar, L. *et al.* (2016) ‘Optimizing imaging conditions for demanding multi-color super resolution localization microscopy’, *PLoS ONE*, 11(7), pp. 1–18.

Sengupta, P. *et al.* (2011) ‘Probing protein heterogeneity in the plasma membrane using PALM and pair correlation analysis’, *Nature Methods*, 8(11), pp. 969–975.

Sengupta, P., Jovanovic-Talisman, T. and Lippincott-Schwartz, J. (2013) ‘Quantifying spatial organization in point-localization superresolution images using pair correlation analysis’, *Nature Protocols*, 8(2), pp. 345–354.

Veatch, S. L. *et al.* (2012) ‘Correlation functions quantify super-resolution images and estimate apparent clustering due to over-counting’, *PLoS ONE*, 7(2). doi: 10.1371/journal.pone.0031457.

Yang, W. *et al.* (2016) ‘Regulation of Meristem Morphogenesis by Cell Wall Synthases in Arabidopsis’, *Current Biology*, 26(11), pp. 1404–1415.

Zhao, Z. W. *et al.* (2014) ‘Spatial organization of RNA polymerase II insidea mammalian cell nucleus revealed by reflectedlight-sheet superresolution microscopy’, *Proceedings of the National Academy of Sciences of the United States of America*, 111(2), pp. 681–686.